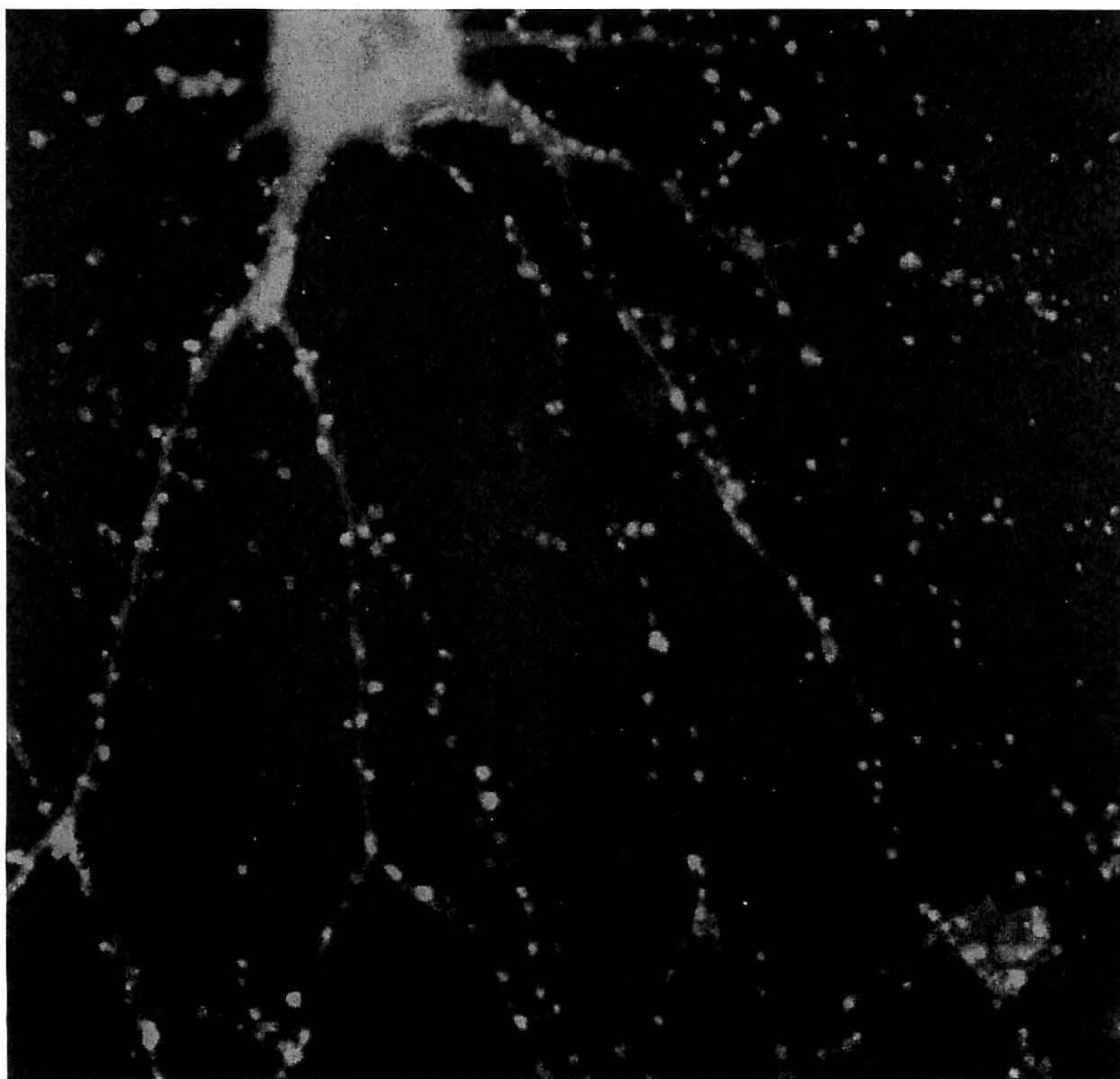


Caltech
Undergraduate
Research
Journal

1996



Vol. 1, No. 1

Table of Contents

Gene Expression and Protein Localization in <i>Leishmania</i> Saurabh Saha, Levi A. Garraway, & Stephen M. Beverley	2
Novel Complexes of Osmium as Molecular Probes for DNA: Preparation and Characterization Johanna A. Yao, R. Erik Holmlin, & Jacqueline K. Barton	5
Progress Towards the Structural Elucidation of Molecular Recognition Anandi Raman, Pamela J. Bjorkman & Roland K. Strong	9
Incorporation of Caged Compounds into the Acetylcholine Receptor Jeffrey C. Miller and Henry A. Lester	12
Colocalization of α CaMKII and PSD-95 in the Postsynaptic Density Jason C. Lee and Mary B. Kennedy	16
The Expression and Functional Analysis of Mammalian Olfactory Receptor Hoai-Ky Vu Ho, Yinong Zhang, Henry A. Lester, & Kai G. Zinn	20
Colocalization of Postsynaptic Density Proteins α CaMKII and NR2B in Dissociated Hippocampal Neurons Lin Z. Jia and Mary B. Kennedy	23
Bidding for Computer Time Minneola P. Ingersoll, David Krider, Andrew Ingersoll, & Scott E. Page	26
Lattice Gas Cellular Automata with Almost Periodic Initial Conditions Evan Reed	31
Bell Numbers and k-Trees, and Drawing and Ordering of Trees Winston Yang and Richard M. Wilson	34
Inflatable Structures Technology Farouk Hadeed and Joel C. Sercel	36

Dear Readers,

Most of the undergraduates at Caltech came here not only for its pranks and its stimulating environment, but also to take advantage of the excellent opportunity to participate in its world-class research. The SURF Student Advisory Council (SURFSAC) created this journal to give an account of some of the best research done by undergraduates at Caltech. The articles herein have passed through a rigorous review process in which comments and suggestions were offered by the CURJ Student and Faculty Editors. We have strived to target the journal toward both the technical and non-technical audience by selecting the articles which were scientifically interesting and understandable to the public.

Although many of the submissions were of high quality and deserved to be published, due to cost limitations we are able to publish only a dozen of the papers. Nonetheless, we feel that both the authors and we, the editors, have learned a great deal from the process. We hope you find the articles enlightening and enjoyable.

Chou Hung, B.S., 1995
Chair, CURJ Committee

Student Editors

Chou Hung
Mintao Fan
Lin Jia
Diana King
Priyamvada Rai

Faculty Editors

Pamela Bjorkman
Kim C. Border
Charles J. Brokaw
Jerrold E. Marsden
Robert D. McKeown
John D. Roberts

SURFSAC

Jennifer Miller, Chair
David Cuthbert
Amanda Eckermann
Heidi Eldenburg
Mintao Fan
Chou Hung
Lin Jia
Brian Kim
Diana King
Jason Lee
Priyamvada Rai
Anandi Raman
Kate Talmazan
David Wang
Eileen Wexler
Jian Zhang

Design by the CURJ Committee

Layout by Chou Hung

*Published by the Caltech Summer Undergraduate Research Fellowship Office
October 19, 1996*

Gene Expression and Protein Localization in *Leishmania*

Saurabh Saha, Levi A. Garraway*, & Stephen M. Beverley*

* Department of Biological Chemistry and Molecular Pharmacology, Harvard Medical School, Boston, MA 02115

The protozoan parasite *Leishmania* causes an infectious disease afflicting millions of people worldwide. This parasite undergoes a complex digentic life cycle involving many unique biological processes such as RNA-editing and *trans*-splicing¹. To gain molecular insights into these phenomena, we sought to identify genes selectively expressed and localized to specific parasite organelles. Two *Leishmania* genomic DNA libraries were constructed in pXG1-'GFP, a vector designed to generate translational fusions with green fluorescence protein (GFP)²; fusions so obtained could then be screened for gene expression and protein targeting. *Leishmania* genomic DNA fragments of 8-10 kb, partially digested with either Sau3A or PstI, were ligated into pXG1-'GFP, and libraries of ~700,000 Sau3A *E. coli* clones and ~27,000 PstI *E. coli* clones were obtained. DNA from the PstI library was transfected into *Leishmania*, yielding ~6,000 *Leishmania* clones. From 1006 colonies screened, five fusions were identified. Two of these fusions localized to specific organelles and the remaining three were cytoplasmic. Gene fusions obtained from these screens may be characterized further to determine their possible roles in *Leishmania* biology and pathogenesis.

Background on *Leishmania*

The protozoan *Leishmania* is an asexual eukaryotic diploid belonging to the family of Trypanosomatidae. *Leishmania spp.* have a small genome of approximately 50,000 kilobases (kb) with 25-30 small chromosomes. The protozoan provides insight into unique molecular phenomena such as mitochondrial RNA editing and *trans*-splicing. The digentic parasite is carried in the gut of a phlebotomine sand fly as a flagellated promastigote, which is the stage of life useful to us in the project. When the promastigote enters the host, it differentiates into an

amastigote which resides in vertebrate macrophages. The life cycle commences again when a sand fly ingests amastigotes from the host. This human pathogen is able to evade host defense mechanisms by implementing various forms of survival. The virulent *Leishmania*, depending on the species, can cause mild cutaneous lesions, a mucutaneous disease, or a deadly visceral infection. Although there are methods for treating the parasite, such as pentavalent antimony complexes and plant (*Ricinus communis*) biological controls, there remains a need to improve disease fighting drugs to help the 12 million people affected worldwide by this tropical disease. To achieve a better understanding about *Leishmania* biology and pathogenesis, we developed a method by which gene expression and protein localization might be studied in *Leishmania*. The method required the construction of a *Leishmania* genomic DNA library in an expression vector which would create gene fusions to GFP, thereby allowing genetic screens to be accomplished. The execution of the experiment consisted of two phases: the construction of the *Leishmania* genomic DNA libraries and the screening for gene fusions.

Construction of the BamHI/Sau3A and Sse8387/PstI Libraries

Features of pXG1-'GFP

The pXG1-'GFP translational fusion vector (FIG. 1) contains several attractive features for constructing a genomic library that will yield gene fusions. Because there is no ATG codon on its GFP open reading frame, the GFP protein can only be expressed in *Leishmania* if an ATG (codon) and a splice acceptor are provided by the insert DNA. A polylinker site 5' to the GFP cassette facilitates subcloning of a variety of genomic fragments upstream of GFP. A beta-lactamase gene *colE1* origin, and a neomycin resistance gene flanked by *Leishmania* sequences allow pXG1-'GFP to function as a shuttle vector between *E. coli* and *Leishmania*³.

Preparation of Vector DNA

The vector DNA was prepared by growing a single bacterial colony containing pXG1-'GFP in broth containing ampicillin. When purifying the vector, multiple phenol/chloroform extractions were performed to achieve the cleanest possible DNA. After quantifying the DNA via spectrophotometry and gel electrophoresis, the DNA was digested with either BamHI or Sse8387⁴. The efficiency of enzyme digestion was determined via gel electrophoresis. Only one digestion with Sse8387 was necessary to digest the vector completely. However, two digestions with BamHI were necessary to eliminate undigested DNA, as determined via electrophoresis. Each vector was then phosphatased to eliminate self-ligation during the ligation reaction with genomic DNA. The digested and phosphatased DNA was gel-purified overnight to resolve away any undigested DNA that may have been undetected. After gene-cleaning the vector DNA, control ligations were performed to determine if the DNA was digested and

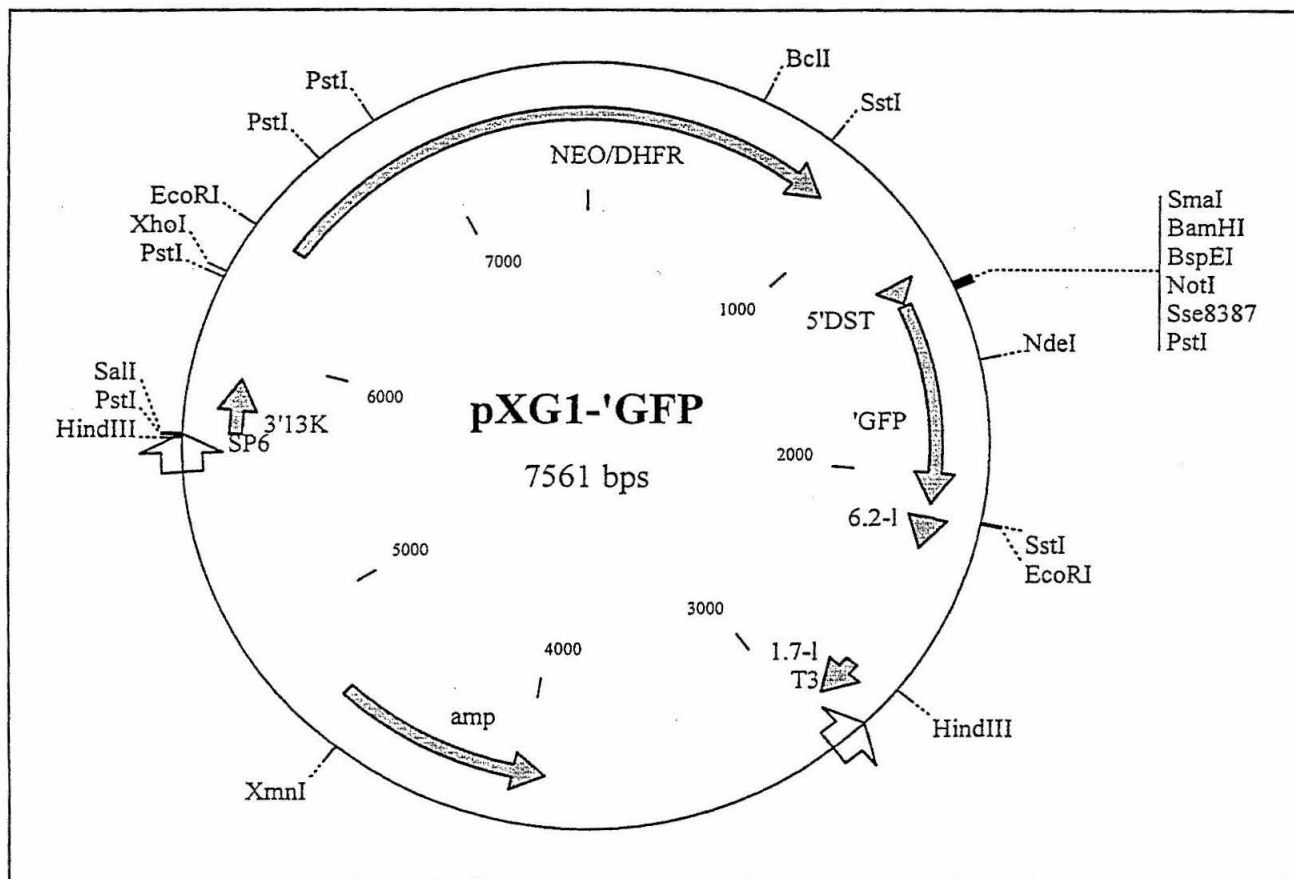


FIG. 1. pXG1-'GFP vector

phosphatased efficiently. Two sets of controls assessed phosphatase efficiency: 1) cut unligated vector and 2) cut self-ligated vector. After phenol/chloroform extraction, the ligation reactions were introduced into *E. coli* via electrotransformation. The vector cut with PstI yielded few colonies with the same number of colonies on both the self-ligated and unligated plate, indicating that the vector was digested and phosphatased efficiently. However, the vector digested with BamHI, which also yielded few colonies, had significantly more colonies on the self-ligated plate compared to the unligated plate. Therefore, a second phosphatase reaction was performed on the vector. After repeating the test above, both the unligated and self-ligated vectors yielded same number of colonies. When both vectors passed the test outlined above, they were ready for use in constructing the libraries.

Preparation of Leishmania Genomic DNA

To obtain the *Leishmania* DNA, genomic DNA from *Leishmania Major* Friedlin V1 was prepared after growing the cells to late log phase. After alkaline lysis, the DNA was spooled out of the tube and washed several times. Multiple phenol/chloroform extractions were performed until no protein interface was visible to assure cleanest

possible DNA. A minigel was run to assess recovery, and the genomic DNA was quantified by the spectrophotometer. Since genomic DNA fragments from a size range of 8-10 kb were necessary to build the libraries, partial digestion with the enzymes PstI or Sau3A (the compatible enzymes of Sse8387 and BamHI respectively) were performed⁵. A gel of the partial digestions was run and a smear of DNA from low to high molecular weight was achieved. After the DNA fragments of the correct size were excised from the gel and gene cleaned, a minigel was run with the digested/phosphatased vector DNA to determine genomic DNA recovery and the optimal ratio of vector DNA to genomic DNA for the ligation reactions.

Ligation and Transformation of Vector and Genomic DNA

After obtaining both the vector DNA and the genomic DNA, the two were combined in ligation reactions. For the Sse8387/PstI combination, a one to seven ratio of vector to genomic DNA was ligated which gave significant stimulation after transformation relative to the self-ligated plate. For the BamHI/Sau3A combination, a variety of vector-to-insert ratios (1:1, 1:2, 1:4, 1:7) were ligated, and the optimal ratio of 1:3 was used for making the library. Several controls were included when testing the optimal

efficiency of ligation. The Sse8387/PstI library has a 95%+ efficiency. Similarly, the BamHI/Sau3A library has a 90%+ efficiency.

After transformation, the PstI library was plated on LB agar plates containing 50 µg/ml ampicillin, and ~27,000 independent *E. coli* clones were obtained. To verify that the colonies had inserts, twenty colonies were picked for mini prep analysis. The recovered DNA was digested with HindIII to detect a common band present in the vector. After running the DNA on a gel, all twenty of the colonies picked had inserts as the common band of ~3 kb (FIG. 1) was present in all the vectors and the insert bands of varying sizes were also detectable. After the preliminary BamHI/Sau3A library of ~85,000 clones was shown to have inserts by mini prep, the remaining ligations were transformed and plated on twenty-five large petri dishes which yielded ~600,000 colonies.

Transfection into Leishmania

After preparing the DNA from the pooled Sse8387/PstI library, it was transfected into *Leishmania Major* V1⁶. Sixty-two transfections were performed using ~60 µg of DNA. Several controls were included: pXG1-'GFP (negative control), pXG1-GFP (positive control), and three different strains of pXG1-LPG1-'GFP. After the two week incubation period, ~6000 total colonies were detectable on the plates (>100 colonies per plate).

Screening for Gene Fusions

From 18 *Leishmania* plates, 1006 colonies were picked into eleven 96 well microtiter plates containing 200 µl of M199 with 15 µg/ml of G418⁷. Three days later the cells were passaged into media containing 100 µg/ml of G418. After three days, 10 µl from each well were placed on a slide and visualized under a fluorescence microscope. When shining blue light at ~395 nm through the slide, the control pXG1-GFP *Leishmania* cells fluoresced green⁸. From the 1006 wells screened for cytoplasmic or localized green *Leishmania*, five fusions were found; two localized to a specific organelle and three remained cytoplasmic. The *Leishmania* cells containing fusions were passaged for further study and characterization.

Results and Future Prospects

The experiment has shown that the method of obtaining gene fusions and screening for protein localization can be used successfully to rapidly identify expressed genes and to pinpoint their intracellular localization. An immediate prospect for this project is to sequence the five fusions to identify the genes expressed. Partial sequence of the genes involved can be obtained by recovering the DNA from the *Leishmania* clone with the expressed fusion and sequencing across the gene fusion by using primers

from GFP. To determine if a *Leishmania* gene is being expressed, the sequence would be analyzed for a splice acceptor site and an in-frame ATG. Comparison between the sequence and the genome database may give rise to further insights as to the function and identity of the gene. Functional experiments may be done on the protein depending on the type of protein identified and the organelle to which it localizes. The pooled bacterial library of BamHI/Sau3A could be transfected into *Leishmania*. The *Leishmania* cells may be screened by using the Fluorescence Activated Cell Sorter (FACS), which may be used to do a preliminary screen for fusions. If the FACS is unable to identify cells with localized fusions that have weak fluorescence activity, then the fluorescence microscope may be used. However, modifications to the GFP cassette, in the future, may yield greater fluorescence activity, thereby allowing the FACS to rapidly screen and sort through many cells and identify localized fusions. Data from such screens could be used to identify classes of proteins localized to particular organelles. These proteins could then be analyzed to assess their role(s) in the biological processes occurring in these organelles. Since there are many biological processes that are poorly understood, such as nuclear gene regulation and mitochondrial RNA editing in *Leishmania*, this approach might identify candidate genes involved in these phenomena.

Acknowledgements

I would like to thank the Caltech SURF program and Harvard Medical School for financial support and also the Beverley lab for helpful advice.

References

1. LeBowitz, J. H., Smith, H. Q., Rusche, L., Beverley, S. M., "Coupling of poly(A) site selection and *trans*-splicing in *Leishmania*," *Genes and Development*, Vol. 7, 996-1007, 1993.
2. Chalfie, M., Tu, Y., Euskirchen, G., Ward, W. W., Prasher, D. C., "Green Fluorescent Protein as a Marker for Gene Expression," *Science*, Vol. 263, 802-803, 1994.
3. Ryan, K., Dasgupta, S., Beverley, S. M., "Shuttle cosmid vectors for the trypanosomatid parasite *Leishmania*," *Gene*, Vol. 131, 145-150, 1993.
4. Descoteaux, A., Garraway, L. A., Kathleen, A. R., Garrity, L. K., Turco, S. J. Beverley, S. M., "Identification of Genes by Functional Complementation in Protozoan Parasite *Leishmania*," *Methods in Molecular Genetics*, 32-34, 1994.
5. Ibid, *Methods in Molecular Genetics*, 26-27.
6. Hyde, J. E., *Protocols in Molecular Parasitology*, 333-335, 1993.
7. Ibid, *Methods in Molecular Genetics*, 26-27.
8. Ibid, Chalfie et al.

Novel Complexes of Osmium as Molecular Probes for DNA: Preparation and Characterization

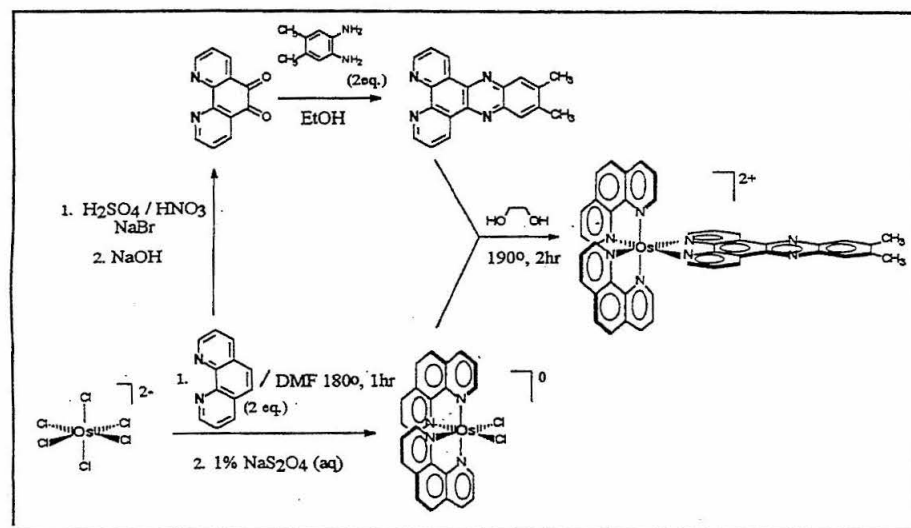
Johanna A. Yao, R. Erik Holmlin, & Jacqueline K. Barton

$\text{Os}(\text{phen})_2(\text{Me}_2\text{-dppz})^{2+}$ ($\text{Me}_2\text{-dppz}$ = 7,8-dimethyl dipyrdo [3,2-a; 2',3'-c] phenazine), a derivative of $\text{Os}(\text{phen})_2\text{dppz}^{2+}$, has been prepared and characterized. In aqueous buffer the complex exhibits no steady-state emission. However, in the presence of double-helical DNA, intense, long-wavelength emission ($\lambda_{\text{max}} = 732 \text{ nm}$) is observed, providing a new osmium based molecular light switch for DNA. Time correlated single photon counting reveals a biexponential decay in emission ($\tau_1 = 2.18 \text{ ns}$, $\tau_2 = 10.1 \text{ ns}$) for the racemic complex bound to DNA by intercalation. We are now exploring the binding of the Δ - and Λ - $\text{Os}(\text{phen})_2(\text{Me}_2\text{-dppz})^{2+}$ to the chiral DNA double helix. $\text{Os}(\text{DAB})_2(\text{Me}_2\text{-dppz})^{2+}$ (DAB = 4,4'-diamino-2,2' bipyridine) has also been synthesized in order to tune the $3^+/2^+$ redox couple of the metal complex for reactions with DNA.

Introduction

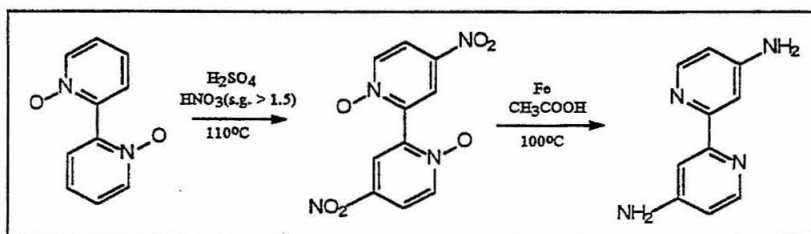
Small molecule probes have contributed greatly to the understanding of nucleic acid structure and function. In the Barton Group, extensive research centers around the use of polypyridyl transition metal complexes as probes for nucleic acids in solution. Mixed ligand complexes of the type $[\text{M}(\text{phen})_2\text{dppz}]^{2+}$ (M = osmium(II), ruthenium(II); dppz = dipyrdo[3,2-a; 2',3'-c] phenazine) have been shown to be molecular light switches for double helical DNA. In the absence of DNA, these compounds show no luminescence in aqueous buffer due to the quenching by hydrogen bonding between water and the phenazine nitrogens of the dppz ligand. Yet, in the presence of DNA, intense photoluminescence is observed as an effect of preferential intercalation that occurs between DNA base pairs and the dppz ligand which provides protection of the phenazine nitrogens from water. This light switch activity is especially sensitive to alterations in ligand structure. By analogy to similar ruthenium complexes, we anticipated modifications of the intercalating ligand to provide a compound with an enhanced quantum yield.

In addition to their potential application in biosensor technology, $[\text{M}(\text{phen})_2\text{dppz}]^{2+}$ complexes are also important in the investigation of DNA mediated electron transfer. Complexes of osmium containing the dppz ligand have provided specialized DNA probes that are active on a fast time scale and exhibit red emission. By incorporating simple modifications in the ancillary phen or bpy ligands, the $3^+/2^+$ redox couple of the metal complex can be tuned. The preparation of a series of complexes spanning a range of redox energies will enable us to evaluate the role this property plays in DNA mediated electron transfer. As part of an ongoing effort to explore DNA mediated electron transfer using novel DNA probes, we have begun the synthesis and characterization of new polypyridyl complexes containing osmium.



Scheme 1. Strategy for synthesis of $\text{Os}(\text{phen})_2(\text{Me}_2\text{-dppz})^{2+}$

Scheme 2. Preparation of 4,4'-Diamino-2,2'-bipyridine (DAB)



Results

Synthesis of $\text{Os}(\text{phen})_2(\text{Me}_2\text{-dppz})^{2+}$

Since $\text{Os}(\text{phen})_2(\text{Me}_2\text{-dppz})^{2+}$ represents a novel compound, we first developed a strategy for synthesis, shown in Scheme 1. ^1H NMR, UV-vis and MALDI TOF MS were used to physically characterize the complex and were carried out until a satisfactory structure of $\text{Os}(\text{phen})_2(\text{Me}_2\text{-dppz})^{2+}$ was confirmed. Impurities were then rigorously excluded by alumina column (acetonitrile eluent) and HPLC. Also, the Δ - and Λ - forms of $\text{Os}(\text{phen})_2(\text{Me}_2\text{-dppz})^{2+}$ are currently being resolved.

Synthesis of 4,4'-Diamino-2,2'-bipyridine

As a part of an ongoing effort to explore DNA-mediated electron transfer using novel osmium complexes, we have also synthesized a new ligand that will help us tune the $3^+/2^+$ redox couple of the metal for reactions with DNA. Using a method for the synthesis of disubstituted bipyridines described by Maerker and Case¹, we prepared 4,4'-Diamino-2,2'-bipyridine (DAB) shown in Scheme 2. This new ancillary ligand and the (Me₂-dppz) ligand are currently being attached to the osmium metal center to obtain the desired $\text{Os}(\text{DAB})_2(\text{Me}_2\text{-dppz})^{2+}$ (FIG. 1).

Steady-State Emission

Figure 2 shows the steady-state emission profiles of $\text{Os}(\text{phen})_2(\text{Me}_2\text{-dppz})^{2+}$ in buffered aqueous solution and in the presence of double stranded DNA. No detectable emission was observed in the buffered solution upon

irradiation at 480 nm. Yet, upon the addition of DNA a dramatic long wavelength emission ($\lambda_{\text{max}} = 732 \text{ nm}$) was observed leading to the conclusion that $\text{Os}(\text{phen})_2(\text{Me}_2\text{-dppz})^{2+}$ was a new molecular light switch for DNA. Based on the steady-state emission from $\text{Os}(\text{phen})_2(\text{Me}_2\text{-dppz})^{2+}$ bound to DNA, we estimate a quantum yield for emission (Φ_{em}) of 0.0002. This Φ_{em} for $\text{Os}(\text{phen})_2(\text{Me}_2\text{-dppz})^{2+}$ is twice that of the $\text{Os}(\text{phen})_2\text{dppz}^{2+}$ parent.

Time Resolved Luminescence Decay

The excited state lifetimes of $\text{Os}(\text{phen})_2(\text{Me}_2\text{-dppz})^{2+}$ with sonicated calf-thymus DNA were measured by time-correlated single-photon counting (TCSPC). Figure 3 shows the luminescence decay with DNA.

Characterization of Intercalation by Visible Spectroscopy

Figure 4 shows the effect of increasing calf-thymus DNA concentration on the $\text{Os}(\text{phen})_2(\text{Me}_2\text{-dppz})^{2+}$ visible absorption spectrum. As DNA concentration is increased, pronounced hypochromism is observed in the intraligand (IL) band as well as the MLCT transitions, with an isosbestic point at 321 nm. There is a 37% decrease in absorbance at 383 nm and a red shift of 6 nm in the IL band. Similar trends in shifting and hypochromism have also been seen in poly(dG-dC) and poly(dA-dT).

Cyclic Voltammetry

Cyclic voltammetry (CV) was used to characterize the oxidation and reduction potentials of $\text{Os}(\text{phen})_2(\text{Me}_2\text{-dppz})^{2+}$

FIG. 1. $\text{Os}(\text{DAB})_2(\text{Me}_2\text{-dppz})^{2+}$

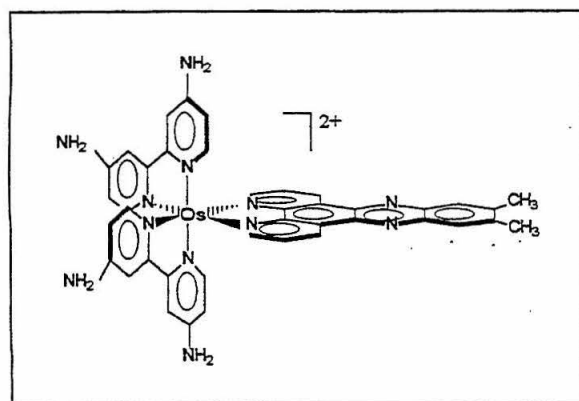


FIG. 2. Steady-state emission spectrum of $\text{Os}(\text{phen})_2(\text{Me}_2\text{-dppz})^{2+}$

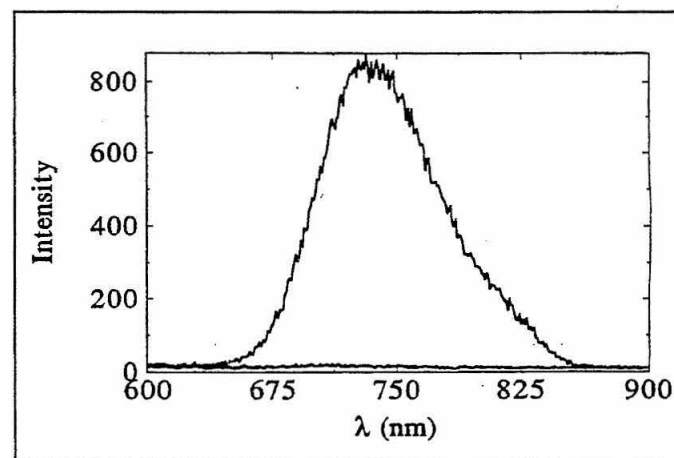


FIG. 3. Luminescence decay profile of $\text{Os}(\text{phen})_2(\text{Me}_2\text{-dppz})^{2+}$ in sonicated calf thymus DNA

A biexponential decay in emission is observed when the complex intercalates into DNA ($\tau_1 = 2.18$ ns, $\tau_2 = 10.1$ ns). This data is consistent with two intercalation binding modes of the complex to DNA.

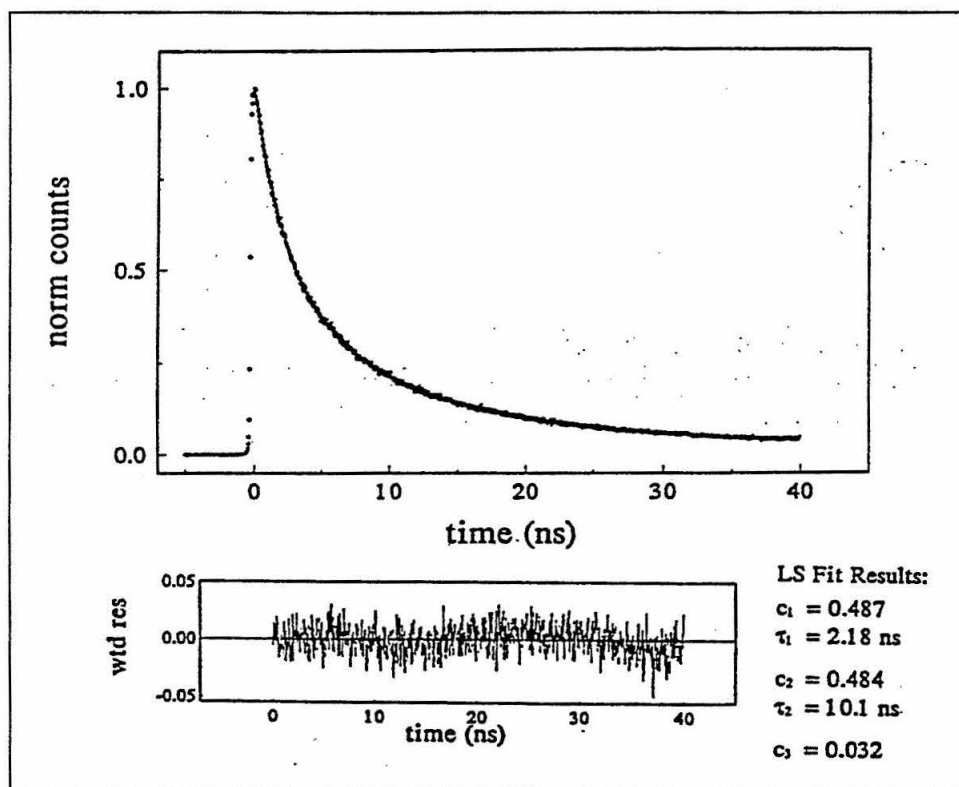


FIG. 4. Visible absorption spectra of racemic $\text{Os}(\text{phen})_2(\text{Me}_2\text{-dppz})^{2+}$ ($35 \mu\text{M}$ Os, 3 mM Tris, 50 mM NaCl, pH 8.5) in increasing concentrations of calf thymus DNA

Ratios of [DNA nucleotide]/Os shown are as follows: 0, 43.75, 58.45, 87.5, 115.5, 140, 245.

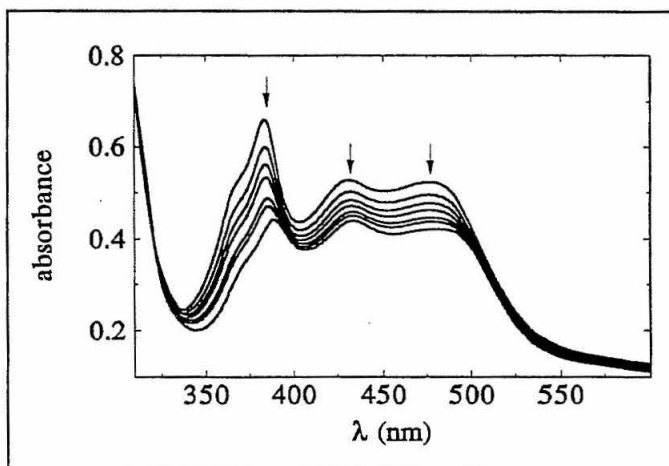
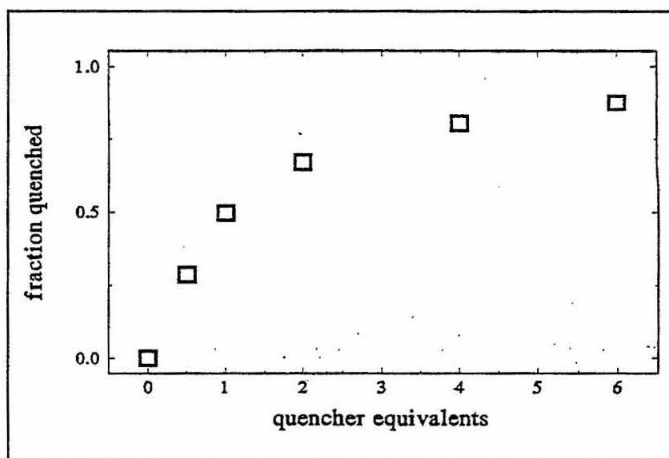


FIG. 5. Quenching of $\text{Os}(\text{phen})_2(\text{Me}_2\text{-dppz})^{2+}$ by $\Delta\text{-Rh}(\text{phi})_2\text{bpy}$ equivalents



dppz)²⁺. A reversible oxidation wave corresponding to the 3⁺/2⁺ couple is observed at 1.165 V (*vs* NHE). This redox couple occurs at the same potential in Os(phen)₂(Me₂-dppz)²⁺ as in Os(phen)₂dppz²⁺. This indicates a weak, if any, interaction between the phenazine portion of the ligand and the metal center. Reductions are observed at -0.705 V, -1.005 V, and -1.24 V (*vs* NHE). By analogy to the reduction of Ru(bpy)₂dppz²⁺ and Os(phen)₂dppz²⁺ measured by CV, the reduction at -0.705 V is assigned to a one-electron reduction centered on the dppz ligand, or in this case the Me₂-dppz ligand, while the two remaining reductions correspond to one-electron reductions on the phenanthrolines. These values are very similar to those of the parent complex. Further, the reduction potentials of Os(phen)₂(Me₂-dppz)²⁺ are consistent with CV data for other polypyridyl complexes of ruthenium and osmium. This important relation indicates a similar absolute energy for the HOMO in the M(phen)₂L²⁺ (M = Os(II), Ru(II); L = Me₂-dppz, dppz) MLCT excited states.

Electron Transfer Study

We are interested in determining the effect of the DNA Π -stack on the reactivity of metal complexes, in particular electron transfer. Emission from intercalated Os(phen)₂(Me₂-dppz)²⁺ is strongly quenched by electron transfer to Δ -Rh(phi)₂bpy (phi = 9,10-phenanthrene quinone diimine)². In order to investigate this quenching over a range of rhodium concentrations, we carried out a quenching titration. The results of such a titration are shown in Figure 5. At 0.5 equivalents of Δ -Rh, 30% of the osmium is quenched while at 5 equivalents of Δ -Rh, 90% of the emission is quenched. Interestingly, the efficiency of this

electron transfer is greater than that of the parent rac-Os(phen)₂dppz²⁺ and comparable to the quenching of Δ -Os(phen)₂dppz²⁺. A full characterization of the forward and back electron transfer reactions between Os(phen)₂(Me₂-dppz)²⁺ and Δ -Rh(phi)₂bpy bound to DNA is currently underway.

Conclusion

We have begun a program to develop osmium complexes as novel DNA probes. A versatile synthetic scheme for the preparation of Os(phen)₂(Me₂-dppz)²⁺ has been established and carried out. The complex has been shown to be a molecular light switch for DNA by luminescence experiments, emitting in the red and active on a fast time scale. The 4,4'-Diamino-2,2'-bipyridine ligand has been prepared and is currently being attached to the osmium metal center with Me₂-dppz in order to tune the redox couple of the complex for future reactions with DNA. The oxidation and reduction potentials of the complex have been determined by CV. Os(phen)₂(Me₂-dppz)²⁺ has been shown to be active in electron transfer with Δ -Rh(phi)₂bpy, and a full characterization of this process is underway. Finally, the complex's intercalation characteristics with several types of DNA (calf-thymus, poly(dA-dT), and poly(dG-dC)) have been explored by UV-visible spectroscopy.

References and Notes

1. Maerker, G. and Case, F. H., *J. Amer. Chem. Soc.*, Vol 80, 2745, 1958.
2. Transient absorption measurements confirm the formation of the Os(III) electron transfer intermediate.

Progress Towards the Structural Elucidation of Molecular Recognition

Anandi Raman, Pamela J. Bjorkman & Roland K. Strong*

* Fred Hutchinson Cancer Research Center
Seattle, WA 98104

X-ray crystallography is a powerful method used to determine the three-dimensional structures of proteins, and it is dependent upon the purity of the protein used for crystallization. I have concentrated on two molecules involved in protein-protein recognition: the tumor suppressor p27 and J chain. p27 binds to and inactivates cyclin E-cdk2 complexes. I have purified the protein and have begun the initial crystallization trials. J chain is a small polypeptide associated with IgA dimers, and is thought to be involved in IgA transport across the epithelium. I have constructed two expression vectors for yeast-based and baculovirus-based expression systems for J chain.

Introduction

One method to determine protein structure is X-ray crystallography. A protein of biological interest is chosen and crystals are grown. Well-ordered, large crystals are bombarded with X-rays and the diffraction patterns recorded. This method is repeated with proteins complexed to heavy atom derivatives, and the two sets of data are compared to yield the amplitudes and phases of the diffracted waves. This technique is called multiple isomorphous replacement. From these data, an electron density map can be constructed. The accuracy of the map depends on the resolution of the diffraction data, which in turn depends on how well-ordered the crystals are. At high resolutions, the known primary sequence of the protein can be fit to the electron density map, with reasonably correct positioning of the amino acid side chains. This yields the three-dimensional structure of the protein.

Growing protein crystals is not an easy task. A variety of conditions must be tried to obtain well-ordered, sizable crystals. Thus, a large amount of the protein of interest must be purified. Recombinantly-expressed proteins are produced in the amounts necessary for crystallization trials, and several purification steps are

MSNVRVSNNGS	PSLERMDARQ	ADHPKPSACR	30
NLFGPVNHEE	LTRDLEKHCR	DMEEASQRKW	60
NDFDQNHKPL	EGRYEQEVE	RGSLPEFYR	90
PPRPPKSACK	VLAQESQDVS	GSROAVPLIG	120
SQANSEDRHL	VDQMPDSSDN	QAGLAEQCPG	150
MRKRPAEDS	SSQNKRANRT	EENVSDGSPN	180
AGTVEQTPKK	PGLRRQT		197

FIG. 1. Amino acid sequence of murine p27, with cysteine residues marked

usually required to produce a homogeneous sample suitable for crystallization.

Crystallization parameters include nature and amount of precipitating agent, co-precipitant, and reducing agent; pH, temperature, and protein concentration. Testing every combination of those conditions would be impossible, so factorial screens are used in the initial trials to narrow down the search for the appropriate conditions. A factorial is a way to evenly sample the n-dimensional crystallization parameter space. The Strong lab uses a custom crystallization factorial consisting of 120 different conditions, as well as two commercially available screens. Once promising results are obtained from the factorial screen, those conditions can be fine-tuned to yield larger, more ordered crystals. The protein will form an amorphous precipitate under many different conditions, and this too can yield important information about the preferred crystallization conditions. For example, changing the pH or temperature could cause the protein to crash out of solution more slowly, in a crystalline form rather than an amorphous one.

Once sizable crystals have been obtained, the X-ray diffraction experiments are then performed. The bulk of the work in structure determination is in the expression, purification, and crystallization of the protein.

I. p27 and Molecular Recognition

The Strong lab is interested in the process of molecular recognition. p27 is a tumor suppressor that controls cell division by binding to cyclin E-cdk2 complexes, which arrests cells in the G1 phase of the cell cycle¹. The three-dimensional structure of p27 may give an indication of exactly how the protein inhibits phosphorylation of cdk2, which is the "go" signal for the cell cycle to proceed past the G1 checkpoint. The structure of a cyclin A-cdk2 complex has recently been determined². Since p27 is known to bind to all cyclin-cdk complexes, a structure of p27 alone could be docked into the known cyclin A-cdk2 structure using computer modeling, in order to study the interactions between the proteins.

In its amino acid sequence, p27 has four cysteine residues which are prone to forming both inter- and intramolecular disulfide bonds (FIG. 1). The Roberts lab, also at the Fred Hutchinson Cancer Research Center, provided the Strong lab with recombinantly-expressed p27

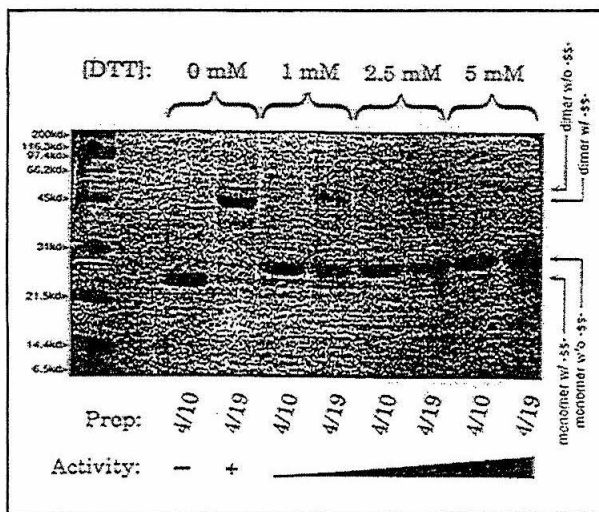


FIG. 2. DTT Treatment of p27

with a six-histidine tag, purified on a Ni²⁺-NTA column. Since completely pure protein is needed for crystallization, the p27 was further purified using a Pharmacia Resource S ion-exchange column and a Superdex 200 gel filtration column. Adding increasing amounts of dithiothreitol (DTT), a reducing agent, decreased the amount of inter- and intramolecular disulfide-bonded species (FIG. 2). Activity assays performed by the Roberts lab showed that the protein's inhibitory activity increased as higher concentrations of DTT were added, indicating that the reduced form of the protein is the active one. The protein was then concentrated in the presence of 5mM DTT, and crystallization trials were set up.

Results and Discussion

Two commercially available factorials, Hampton Inc.'s *Crystal Screen I and II*, were used for the initial crystallization trials, and they yielded a surprising result. After ten days, nearly all of the conditions produced an oily residue in the protein drop, rather than a precipitate or crystals. Non-reducing SDS-polyacrylamide gel electrophoresis was performed on the p27 used for the trials. Many higher molecular weight species were present in the sample, indicating a high concentration of disulfide-linked p27 monomers, dimers, trimers, and higher multimers. We then treated the protein overnight with 50mM β-mercaptoethanol, another reducing agent, and then purified the reduced p27 over a Superdex 200 preparative gel filtration column equilibrated with 2.5mM iodoacetamide (IAA), which binds irreversibly to thiols and blocks disulfide formation. The high molecular weight species disappears after IAA treatment, even in the presence of 1,10-phenanthroline, an oxidizer (data not shown).

This reduced form of the protein, which was then thought to be homogeneous, was used to set up more crystallization trials. Another strategy employed was keeping the three Resource S ion-exchange column fractions, which eluted at different salt concentrations,

separate. Though all the fractions were p27, we treated each one individually with βME and IAA, and set up the crystallization trials separately. These trials yielded promising results; there was much less oiling, and a few conditions produced a crystalline precipitate. This is progress towards growing crystals, since those conditions can be fine-tuned to set up further trials, which may produce crystals suitable for diffraction.

Conclusion

Progress has been made towards the crystallization of the tumor suppressor p27. A detailed purification scheme has been outlined and promising crystallization conditions have been identified. The initial crystallization factorials were set up, and the next step is to determine which conditions are to be fine-tuned.

II. Expression Vectors for Murine J Chain

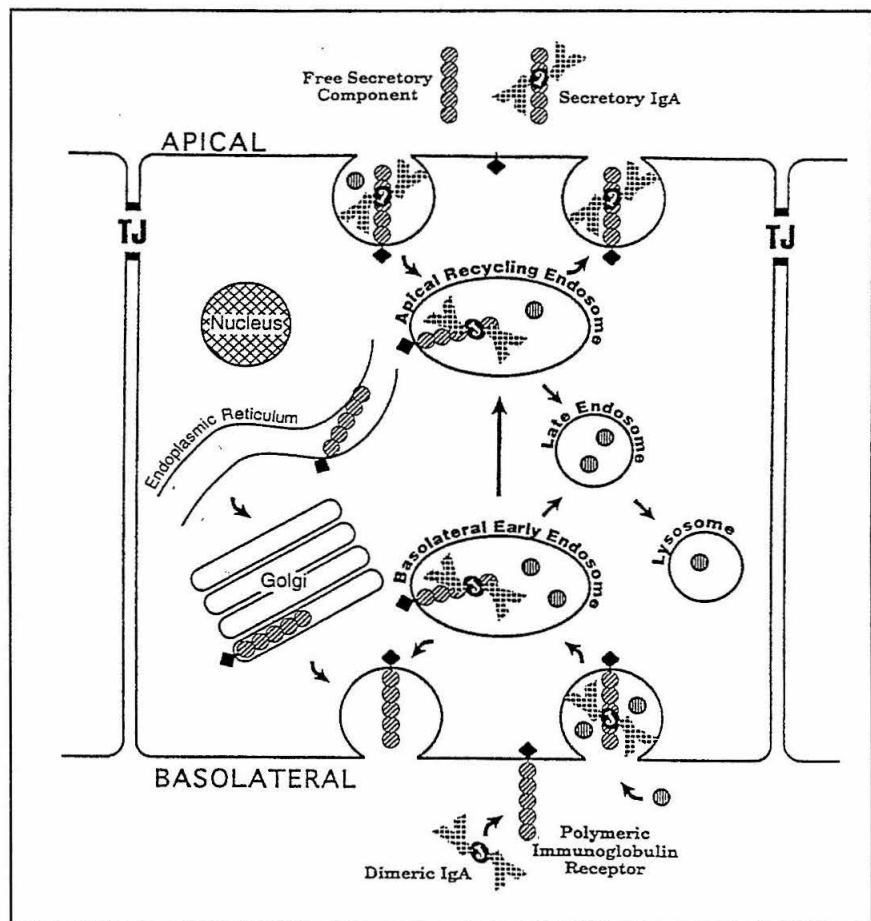
The mammalian immune system is very complex and effective. Included in its arsenal of weapons against invasion by foreign microorganisms and viruses are antibodies, proteins which specifically recognize and bind to molecules on the surface of or secreted by invading pathogens. Antibodies, also known as immunoglobulins, exist in five main classes, which differ in structure, function, and abundance in different locales of the body. One of the isotypes, IgA, tends to associate as a dimer and incorporates an extra polypeptide, known as the J chain.

IgA is the predominant antibody found in the external secretions that coat the mucosal membranes of the body³. There are also significant quantities of IgA in the serum. It is thought that this abundance of IgA at the mucosa makes it the first line of defense against pathogens from the environment that enter through ingestion, inhalation, or sexual contact, but little is known about the overall role of IgA in the immune system⁴.

The primary site of synthesis of IgA antibodies is at the epithelial surfaces of the body. Plasma cells, terminally differentiated to secrete IgA, lie beneath the basement membrane of epithelia. Transport of dimeric IgA across the epithelium into the gut or bronchi is necessary for the molecules to protect the outer surfaces of the GI and respiratory tracts. The process is known as transcytosis, and it involves newly synthesized IgA (including J chain) binding to a protein called the poly Ig receptor (pIgR) on the basolateral side of the epithelial cell. The pIgR-IgA complex is internalized in a vesicle in the cell and transported across the cytoplasm to the apical side. Hydrolytic cleavage of pIgR releases dimeric IgA, still bound to part of the pIgR, into the extracellular space (FIG. 3).

The Strong lab is interested in the molecular recognition between IgA and J chain, as well as that between J chain and pIgR. Since large protein complexes are extremely difficult to crystallize, portions of these complexes are targeted for crystallization. One portion is the murine J chain.

FIG. 3. Transcytosis of IgA



Results and Discussion

We obtained the cDNA for the murine J chain, and used PCR to amplify the sequence and add the FLAG peptide, which simplifies purification of the overexpressed protein. This sequence was then subcloned into the plasmid vector pHIL-S1, which can be used in the *Pichia pastoris* yeast-based expression system. After purification of the J chain-pHIL-S1 vector, the fragment containing the insert was excised and ligated into the baculovirus expression vector pFASTBAC1. This was also purified, and both vectors are now ready for their respective expression systems. J chain can then be expressed, the protein purified, and crystallization trials set up again, to begin the cycle of structure determination.

References

1. Elledge, S.J. and Harper, J.W., "cdk Inhibitors- On the Threshold of Checkpoints and Development," *Curr. Opin. Cell Biol.*, Vol. 6, 847-852, 1994.
2. Jeffrey, P.D., et al., "Mechanism of cdk Activation Revealed by the Structure of a Cyclin A-cdk2 Complex," *Nature*, Vol. 376, 313-320, 1995.
3. Heremans, J.F., *The Antigens*, Vol. 2, 365-522, 1974.
4. Kraehenbuhl, J-P. and Neutra, M.R., "Molecular and Cellular Basis of Immune Protection of Mucosal Surfaces," *Physiol. Rev.*, Vol. 72, 853-879, 1992.
5. Hopp, T. P., et al., "A Short Polypeptide Marker Sequence Useful for Recombinant Protein Identification and Purification," *Biotechnology*, Vol. 6, 1205-1210, 1988.

Incorporation of Caged Compounds into the Acetylcholine Receptor

Jeffrey C. Miller and Henry A. Lester

I have successfully utilized the nonsense codon suppression method for unnatural amino acid incorporation to insert a caged tyrosine in place of wild-type tyrosine of mouse nicotinic acetylcholine receptor α -subunit. The α -subunit mutants, as part of functional receptors, were expressed in *Xenopus* oocytes by coinjecting (1) α tyr198TAG or α tyr93TAG mutant mRNA and (2) a nonsense suppressor tRNA aminoacylated with the photolabile caged tyrosine derivative tyr(ONV). The viability of BPOC as a pH-sensitive protecting group for the amino terminus of an aminoacyl-tRNA was established by incorporation of phenylalanine at α 198, as shown by electrophysiology. Successful incorporation of the caged tyrosine was determined by analyzing oocytes that had been irradiated after protein expression.

Introduction

Proteins that form ion channels in cell membranes are responsible for a great variety of biological functions. The recently developed technique of unnatural amino acid incorporation in intact cells (FIG. 1), pioneered by Nowak et al., 1995, is currently being used to study various aspects

FIG. 1. Unnatural Amino-acid Incorporation in Oocytes

The unnatural amino acid incorporation in intact cells involves coinjecting mutant mRNA and a modified tRNA into a *Xenopus* oocyte. The mRNA is made by run-off transcription of a mutated cDNA clone containing a nonsense codon, TAG, at the position to be altered. The tRNA used is tetrahymena tRNA that has the complimentary anticodon sequence (CUA), with the desired amino acid chemically acylated to the 3' end. The amino acid acylated to the suppressor tRNA is specifically incorporated into the appropriate position in the protein encoded by the mRNA during translation by the oocyte's synthetic machinery. This diagram courtesy of the Lester Lab.

of function and structure of some membrane proteins. A novel addition to this powerful technique would be the insertion of amino acid residues with protecting groups that could be removed after the protein has been expressed in the cell. The protecting group, also called the "caging group", would effectively hide a portion of the protein until the caging group is selectively removed. This technique could allow incorporation of charged residues, which have been difficult to insert with the current method, or incorporation of residues containing biologically active compounds not normally found in proteins. An important variant of the latter would be caged phosphates which could be used to study the effects of phosphorylation and dephosphorylation at specific sites of proteins. If the protecting group could be removed while the channel currents through the oocyte membrane are being measured, the resultant data might give some insights into the function of ionic channels that would be extremely difficult to obtain by other means.

This project explored the possibility of using the unnatural amino acid incorporation technique to specifically incorporate a tyrosine residue, caged as the nitroveratryl ether [tyr(ONV)], into the mouse nicotinic acetylcholine receptor α -subunit. The nicotinic acetylcholine receptor is a well-studied 290 kDa pentamer of similar subunits with two α subunits, a β subunit, a γ subunit, and a δ subunit¹. Copious evidence suggests that residues tyr93, tyr190, and tyr198 of the α subunit are directly involved in agonist binding²⁻⁴, and changes to these residues produce noticeable electrophysiological effects⁵. Acetylcholine, which is the natural agonist to the acetylcholine receptor, was used to induce channel currents across the oocyte membranes in this experiment. The electrophysiological aspect of the incorporated channels measured in this project was the dose-response relation; this is the measured channel current as a function of the agonist concentration. The dose-response relation is a sigmoidal function characterized by a saturating value (I_{MAX}), the concentration of agonist that elicits half

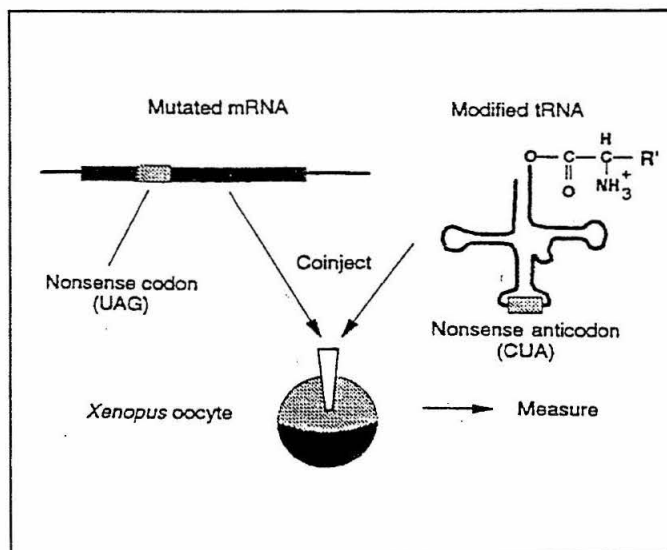
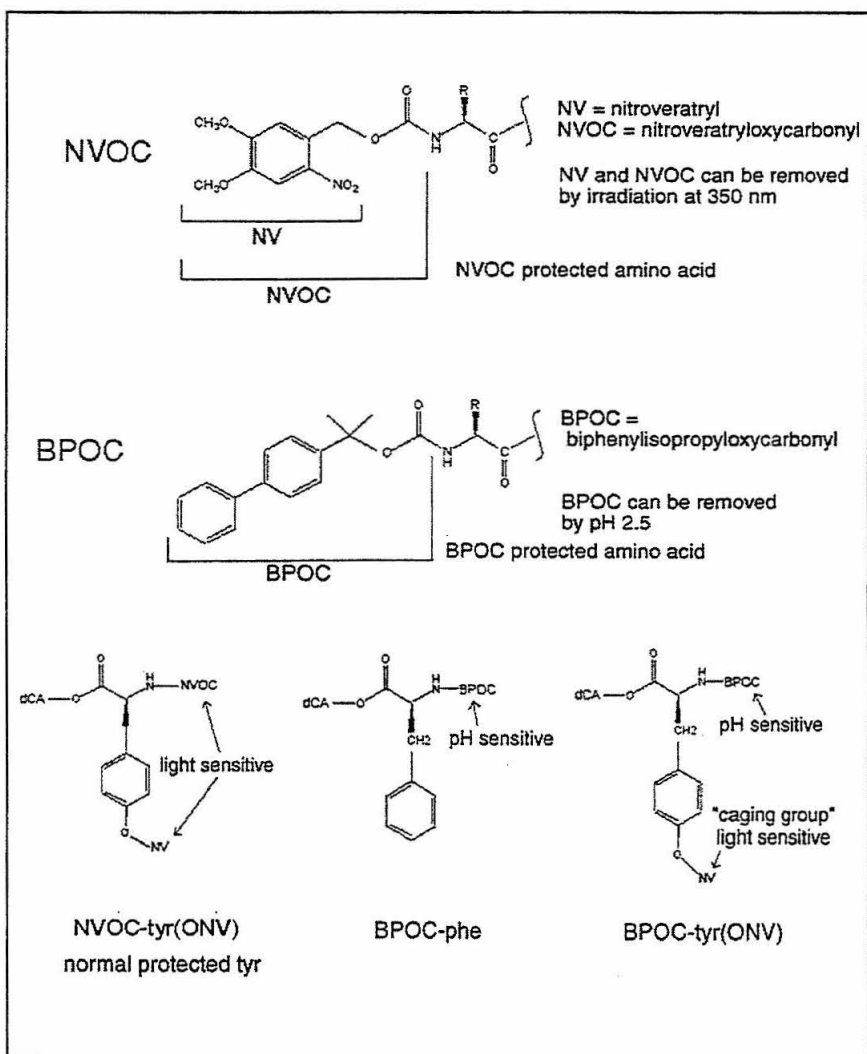


FIG. 2. The structures of the BPOC and NVOC groups and how these groups are linked to the amino acids

The NVOC-tyr(ONV) and NVOC-phe were available from previous studies⁵, but the BPOC-phe and BPOC-tyr(ONV) were synthesized specifically for this project by Scott Silverman of the Dougherty group. The tRNA will attach to the amino acid where the dCA is shown in the diagram.



maximal response (EC_{50}), and the Hill coefficient. From the available evidence (Nowak et al., 1995), caging tyr198 or tyr93 is expected to provide a measurable change in EC_{50} .

The aminoacylated suppressor tRNA ("charged" tRNA) must have a protecting group on the terminal amino group for stability⁶. This protecting group must be removed immediately prior to injection of the tRNA into the oocyte for the amino acid to be incorporated into the protein. The current methodology uses a light-sensitive amino protecting group, but this would remove a light-sensitive caging group and defeat the purpose of the experiment. Therefore an alternate amino protecting group that could be removed without affecting the caging group was pursued. BPOC (biphenylisopropoxyloxy-carbonyl) is a known amine protecting group which can be removed by lowering the pH to 2.5; this was selected for the amino protecting group because it can be removed without affecting the caging group, NV (nitroveratryl), which is removed by irradiation at 350 nm⁷. NV was selected because this group is currently used in conjunction with NVOC (nitroveratryl-oxycarbonyl) to protect amino acid sidechains and terminal amino groups

in the current protocol for unnatural amino acid incorporation. Figure 2 shows the structures of these various protecting groups and how they attached to amino acids.

Presentation and Discussion of Results

The BPOC protecting group on the tRNA terminal amino group must be removed prior to injection. This is accomplished by adding dilute HCl to the tRNA solution lowering the pH to 2.5 and then bringing the pH back to 4.5 with NaOAc prior to injection⁸. There were initial concerns that the tRNA might not function properly after being subjected to the BPOC removal conditions. Tests showed that the tRNA was still functional after being subjected to the BPOC removal conditions (data not shown). The BPOC-protected amino acids were then acylated to tRNA; the resulting compound will be referred to as tRNA-BPOC-phe. The tRNA-BPOC-phe was deprotected by subjecting it to the BPOC removal conditions and then inserted at $\alpha 198$ ⁹. NVOC-phe was also inserted at this position as a control and the experimentally determined EC_{50} 's were compared with the published value of 215 mM⁵. The EC_{50}

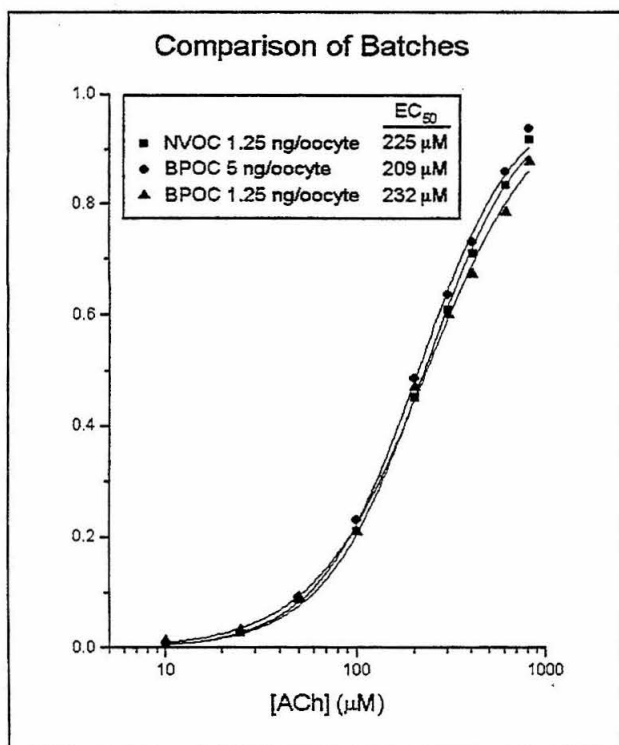


FIG. 3. BPOC-phe vs. NVOC-phe (control)

The same techniques and concentrations that were used for the tRNA sensitivity experiment were used except that the tRNA-BPOC-phe was not photolyzed. The data was fit to the Hill equation, $I/I_{MAX} = 1/(1+(EC_{50}/[A])^H)$ where I is the current for a given agonist concentration $[A]$, I_{MAX} is the maximum current, H is the Hill coefficient. The Hill coefficients, H , were determined by measuring the initial slope on $\log I$ vs. $\log [A]$ plot.

values differ when different residues are incorporated at $\alpha 198^5$ so a similar EC_{50} for BPOC-phe and NVOC-phe will be strong evidence that the BPOC-phe has functioned properly. The results of this experiment are shown in Figure 3. The experimental EC_{50} 's for both the NVOC-phe and BPOC-phe were very close to the published value, but the NVOC-phe gave higher average maximum currents at the same concentration. This fact has been attributed to some of the tRNA-BPOC-phe not containing a BPOC group. The unprotected tRNA would rapidly deacylate; no more fully protected tRNA would be needed to give currents comparable to the control.

Showing that coinjecting tRNA-BPOC-tyr(ONV) with $\alpha 198$ TAG and $\alpha 93$ TAG mutant mRNA yields proteins containing caged tyrosine was much more difficult. If tyr(ONV) is incorporated at $\alpha 198$ or $\alpha 93$, the resultant acetylcholine receptor will either have a different EC_{50} value or will not produce any measurable channel currents when exposed to an agonist. There should also be a noticeable change when the oocytes are irradiated to remove the caging group from any expressed proteins. A control which

consisted of prephotolyzing the tRNA-BPOC-tyr(ONV) in order to remove the caging group was done to test the effects of irradiating the oocytes when no caged residues were in the protein. For unknown reasons irradiating the oocytes seemed to raise their channel currents about 50% (data not shown). This first several times I performed this experiment, I noticed that the currents from oocytes injected with the nonphotolyzed tRNA-BPOC-tyr(ONV) was only about a quarter of that of the oocytes injected with the prephotolyzed tRNA-BPOC-tyr(ONV), but there was no change in the EC_{50} value and the currents in both groups increase by approximately the same amount when the oocytes were irradiated. This suggested that most of the measured current in the experimental batch of oocytes was from proteins that had incorporated tyrosine that had somehow lost their caging group. I then performed some additional trials with the materials for one batch of oocytes handled in a completely ultraviolet-free environment and with an ultraviolet filter on the light on the microscope used to inject the oocytes. The batch of oocytes thus treated had much lower currents prior to photolysis and showed a much greater change upon photolysis, but there was still no change in EC_{50} . This led to the obvious conclusion that the room light or the light on the microscope was actually removing the caging group prior to injection and causing a large background signal that was obscuring the desired signal; it was later determined that the light on the microscope was the major culprit. The average maximum currents (I_{MAX}) from oocytes coinjected with α tyr198TAG mRNA and prephotolyzed control, tRNA-BPOC-tyr(ONV) treated under normal conditions (light-treated), tRNA-BPOC-tyr(ONV) prepared in an ultraviolet-free environment (dark-treated), and dark treated oocytes after having been irradiated for 4 minutes apiece with a 1000W Oriol arc lamp (post-injection photolyzed dark) is shown in figure 4. I was unable to record from enough oocytes from the post-injection photolyzed oocytes injected with prephotolyzed and light-treated material to get reliable average currents in this trial, but previous experiments showed that I_{MAX} for both the post-injection photolyzed oocytes injected with prephotolyzed and light-treated material were approximately 1.5 times greater than the respective non post-injection photolyzed I_{MAX} , and the oocytes from these groups that I did manage to record in the trial shown in figure 4 did not deviate greatly from the previous results. Similar results were obtained with α tyr93TAG mRNA. The fact that the ratio of the post-injection photolyzed dark group was well above 1.5:1 is very strong evidence that at least some protein containing caged tyrosine is being expressed and at least some of the caging group is being removed by photolyzing the oocytes. Ideally the I_{MAX} for the dark-treated batch should be much lower; some photodeprotection of the NV probably occurred at an earlier step in the preparation of the material. The post-injection photolyzed dark batch should also have the same I_{MAX} as the prephotolyzed control batch after oocyte photolysis; some possible causes for this not occurring is that the caged tyrosine could lower protein expression and

the removal of the caging group from the expressed protein by irradiating the oocytes could be incomplete.

Conclusion

The success of the tRNA sensitivity experiments and the BPOC-phe test showed that the scheme of protecting the amino acids with BPOC is viable. While this scheme works, more efficient and less labor intensive schemes are certainly possible and are currently being sought.

The incorporation of caged tyrosine seems to have occurred, but there are still a number of problems with the system. There is still much more background current due to deprotection of the caged residue than is desired, and the yield of functional acetylcholine receptors from oocytes injected with tRNA-BPOC-tyr(ONV) and then photolyzed is rather low. A less bulky caging group that requires stronger UV irradiation to be removed should solve both of these problems. Hopefully these difficulties encountered with the insertion of caged residues into channel proteins can be overcome, thus enabling this technique to live up to its full potential¹⁰.

References and Notes

- Unwin, N., "Acetylcholine Receptor Channel Imaged in the Open State," *Nature*, Vol. 373, 37, 1995.
- Chiara, D. and Cohen, J., "Identification of Amino Acids Contributing to High and Low Affinity d-Tubocurarine (dTC) Site on the *Torpedo* Nicotinic Acetylcholine Receptor (nAChR) Subunits," *Faseb J.*, Vol. 6, A106, 1992.
- Dennis, M., et al., "Amino Acids of the *Torpedo marmorata* Acetylcholine Receptor α Subunit Labeled by a Photoaffinity Ligand for the Acetylcholine Binding Site," *Biochemistry*, Vol. 27, 2346, 1988.
- Galzi J.-L., et al., "Identification of a Novel Amino Acid α -Tyrosine 93 Within the Cholinergic Ligand-binding Sites of the Acetylcholine Receptor by Photoaffinity Labeling," *Journal of Biological Chemistry*, Vol. 265, 10430, 1990.
- Nowak, M. W., Kearney, P. C., Sampson, J. R., Saks, M. E., Labarca, C. G., Silverman, S. K., Zhong, W., Thorson, J., Abelson, J. N., Davidson, N., Schultz, P. G., Dougherty, D. A., Lester, H. A., "Nicotinic Receptor Binding Site Probed with Unnatural Amino Acid Incorporated in Intact Cells," *Science*, Vol. 268, 337, 1995.
- Robertson S. A., Ellman, J. A., Schultz, P. G., "A General and Efficient Route for Chemical Aminoacylation of Transfer-RNAs," *Journal of the American Chemical Society*, Vol. 113, 2722, 1991.
- Ellman, J., Mendel, D., Anthony-Cahill, S., Noren, C., Schultz, P., "Biosynthetic Method for Introducing Unnatural Amino Acids Site-specifically Into Proteins," *Methods in Enzymology*, Vol. 202, 301, 1991.
- The conditions for BPOC removal were to take a solution of tRNA in 1mM NaOAc of volume V at pH 4.5 and add 1/2 V of RNase free 9mM HCl which brought the pH down to 2.5 and wait for 10 minutes. The solution was then brought back up to pH 4.5 by adding 1/2 V of 23mM RNase-free NaOAc made from a 3M stock at pH 5.3.
- The techniques and materials employed were for the most part similar to and described in Nowak et al. with a few major exceptions: the tRNA used in this project was tetrahymena G73 tRNA. All mutant mRNA had 100:1:1:1 ratio of α : β : γ : δ . Recordings were done in ND96 solution (see Nowak et al., 1995 for ion concentrations) with 1 μ M atropine using a Gene Clamp (Axon Instruments) amplifier with KCl filled micropipet electrodes with resistances of 0.5M Ω to 2M Ω .
- I would like to thank Mark Nowak and Scott Silverman for the vast amount of assistance that they gave me on this project. Mark taught me all the relevant laboratory techniques and they both helped with experimental design and data analysis. I would also like to thank SURF for providing funding and the Lester Lab for providing funding, materials, and equipment.

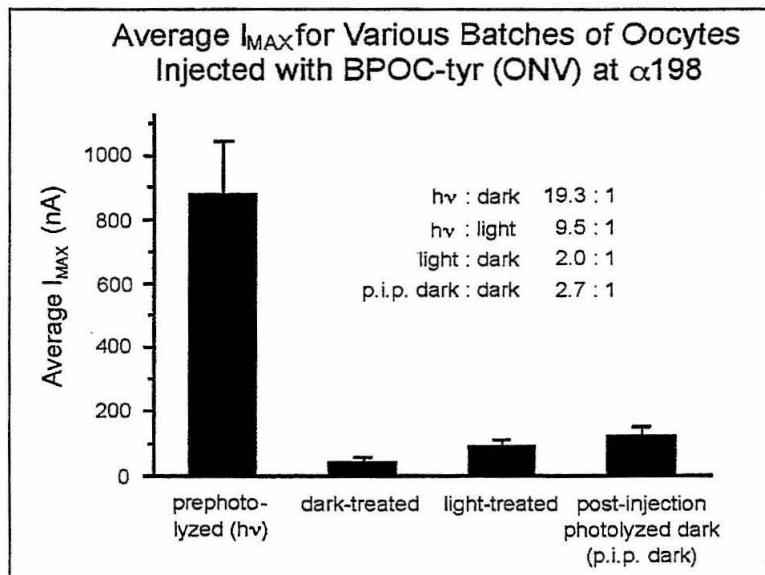


FIG. 4. This is a summary of the data from various batches of oocytes coinjected with *atyr198TAG* mRNA (in a 100:1:1:1 ratio at a concentration of 15.7 ng/oocyte) and BPOC-tyr(ONV) with a concentration of 12.5 ng/oocyte. The batch labeled "hv" was a control and the tRNA-BPOC-tyr(ONV) was photolyzed for 5 minutes with a 1000W Oriel arc lamp prior to injection.

Colocalization of α CaMKII and PSD-95 in the Postsynaptic Density

Jason C. Lee and Mary B. Kennedy

The postsynaptic density (PSD) is a specialized complex of proteins at the postsynaptic membrane of a synapse. It is believed to participate in regulating forms of synaptic plasticity that underlie learning and memory. Biochemical evidence suggests that two proteins, PSD-95 and the α subunit of CaM Kinase II (α CaMKII), are part of the PSD complex. Using immunocytochemical methods, we have confirmed that PSD-95 and α CaMKII are colocalized at neuronal synapses of cell cultures. In addition, we believe that PSD-95 (or an isoform) may be found in glial cells whereas α CaMKII is localized exclusively in neurons. We are presently determining if other proteins believed to be in the PSD colocalize with PSD-95 and α CaMKII.

Introduction

How does the brain function to store memory? This is still a largely unanswered question in the field of neurobiology today. Research advances in the past few decades, however, have given us clues as to how the mechanism of memory storage might work in the central nervous system (CNS). Many scientists believe that it involves changes in junctions between neurons called synapses. The ability for neuronal junctions to change due to variations in signal transmission is called synaptic plasticity. Normally, individual signals transmitted from one neuron at its presynaptic terminal to another neuron at its postsynaptic site have transient effects and are independent of each other. However, in some cases, rapid, successive signals can create what is known as long-term potentiation (LTP)¹. Presynaptic signals following induction of LTP elicit a greater response in the postsynaptic neuron than before LTP. As this phenomenon can last up to several hours in the brain, many believe that LTP contributes to synaptic plasticity and, consequently, to memory formation¹.

The Kennedy Lab focuses on investigation of a particular thickening at the postsynaptic membrane sites called the postsynaptic density (PSD)². It is believed that the PSD has certain regulatory functions during LTP induction and, therefore, can affect long-lasting changes that occur in the synapse². Biochemical studies have indicated

that many important proteins are associated with the PSD²⁻⁵. For example, the α -subunit of Type II Ca²⁺/calmodulin-dependent protein kinase (α CaMKII) is found in the PSD fraction. CaMKII is responsible for activating other proteins by phosphorylation in biochemical pathways in the neurons^{2,3}. Another protein, PSD-95 binds to the carboxyl tail of a glutamate receptor and is believed to regulate synaptic junction formation in neural development^{2,4,6}.

One of the key steps to further clarify the roles of these proteins is the investigation of their localization in the brain. Since we know from biochemical evidence that both PSD-95 and α CaMKII are associated with the PSD², we are interested to know how these two proteins are localized relative to each other throughout a neuronal population. In our investigation, we wish to answer the following questions: 1) Are PSD-95 and α CaMKII colocalized at all postsynaptic terminals of a neuronal cell culture? 2) If not, in what specific combination do they exist at different neuronal synapses?

Procedures

We used dissociated cell cultures from hippocampal tissues of rat brain in our studies. The neurons were grown on a small, plastic coverslip covered with polylysine, for charge neutralization, and laminin, which allowed the cells to cling to the coverslip. The cultures were fed with nutrients for growth and were used in our studies when they were between 2 and 3 weeks old.

For each PSD protein that we were studying, we had available to us primary antibodies that would bind specifically to these PSD proteins when incubated in cell cultures. These antibodies were obtained previously in our lab through immunological methods. We had also available to us, from commercial companies, various types of secondary antibodies that would bind selectively to their target primary antibodies. These proteins are tagged with fluorescent molecules. Upon light excitation of the appropriate wavelength, these molecules emit photons to release energy. We relied on collecting the emission of this light energy to determine the exact location of these molecules. Signals were detected with a Zeiss laser-scanning confocal microscope and collected into computer image files. These images were processed with Photoshop on a Macintosh PowerPC.

Our primary antibody against PSD-95 is called Frances and that against α CaMKII is called 6G9. The secondary antibody against Frances is tagged with Fluorescein, and the secondary antibody against 6G9 is tagged with Cy3. In our experiments, we also used an anti-glial fibrillary acidic protein (GFAP) primary antibody to identify glial cells. The secondary antibody used with that is tagged with Fluorescein.

We determined the colocalizations of the PSD proteins by incubating the antibodies described above in succeeding steps in the neuronal cell cultures. The logic is that since each antibody was specific for its target, we could

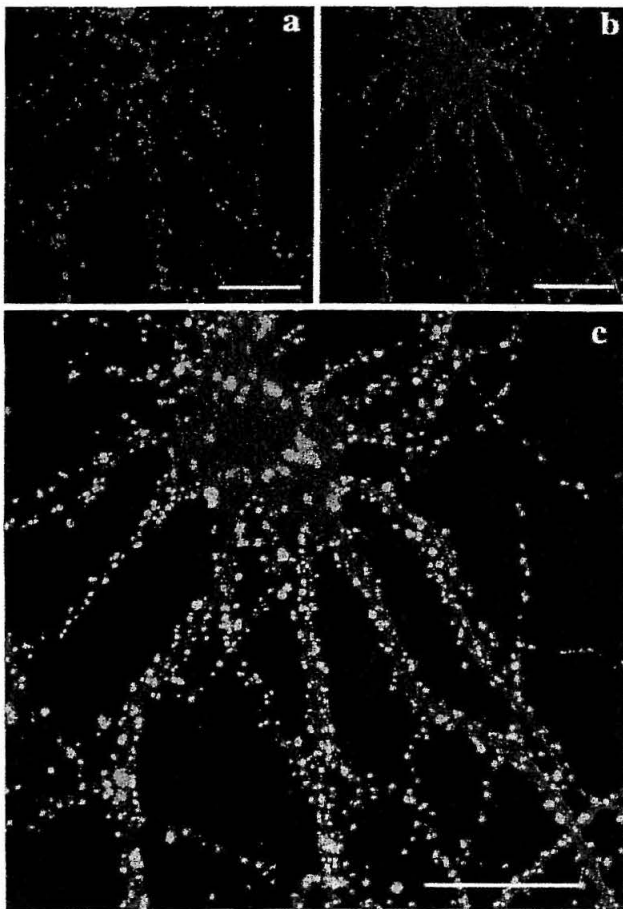
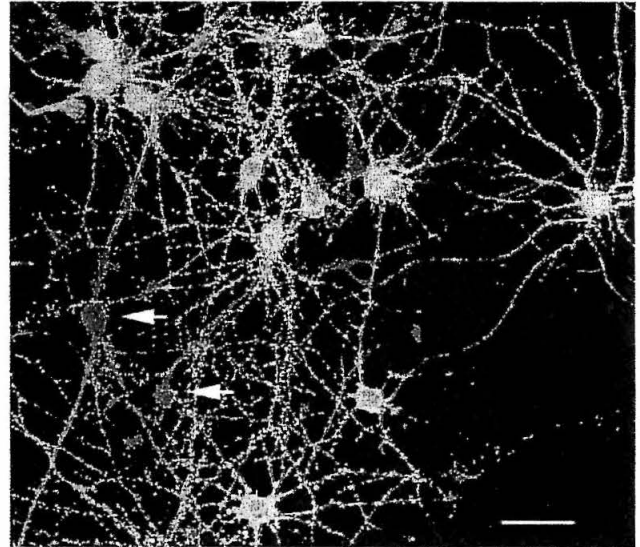


FIG. 1. Double-staining images
 (A) PSD-95 only. (B) CaMKII only.
 (C) Overlay of images A and B. Scale bar is 25 μm .

FIG. 2. Montage of three double-staining single images
 Notice the 3 types of cells: double-stained neurons (yellow cell bodies), PSD-95-stained neurons (green, see arrows), and PSD-95-stained glia (green mesh, in background). Scale bar is 40 μm .



incubate the primary antibodies of both PSD-95 and αCaMKII together, without fearing cross-reaction. The same reasoning held for the secondary antibodies specificity. By examining and determining with a microscope the locations of the fluorescent molecules tagged to the secondary antibodies, we would know precisely the location of primary antibodies that were bound by the secondary antibodies. Since the primary antibodies were also bound to the PSD protein, it followed that the location of the fluorescent molecules essentially defined the location of our PSD proteins.

Experiments were run with single-labeled cell cultures, used to deduce appropriate concentration of antibody dilution, as well as double-labeled cell cultures, used to collect data on colocalization of the proteins. There was always a no-primary culture in each experimental run as control. In any region of the double-stained cultures, images of two different wavelength emissions, corresponding to the two types of fluorescent molecular tags and, hence, the two proteins under investigation, were collected. An image of PSD-95 staining, used with 488 nm wavelength to excite Fluorescein, was processed to a green color. An image of the αCaMKII staining at the same region, determined with the use of a 543 nm wavelength laser to excite Cy3, was processed to a red color. Photoshop was then used to combine the images and to produce montages.

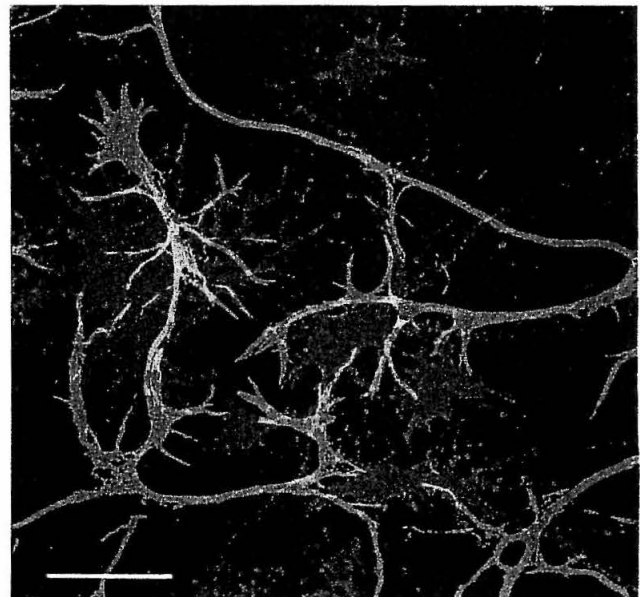


FIG. 3. Double-staining of CaMKII and GFAP
 The red CaMKII outlines the neurons, while the green GFAP outlines the glial cells. Scale bar is 40 μm .

Table 1. Cell type statistics collected from montage

Cell Type	Number of Cells	Percentage
Neurons that are stained for both α CaMKII and PSD-95	41	50%
Neurons that are stained for only PSD-95	3	4%
Glial cells	38	46%
Total	82	100%

Results

Double-Staining Overlay Single Images

Images collected from the first double-staining experiments with 6G9, against α CaMKII, and with Frances, against PSD-95, showed bright dots of staining along neuronal spines, indicating the binding of antibodies for these proteins at the synapses. Since a wavelength of 488 nm excites Fluorescein, which is tagged to the secondary antibody to Frances, the Fluorescein image was processed to green to represent PSD-95 staining. Similarly, since a wavelength of 543 nm excites Cy3, which is bound to the secondary antibody for 6G9, the Cy3 image was collected and processed to red to indicate α CaMKII staining. Upon overlaying the two colored images taken from the same location in a cell culture, any yellow color, a result of combination of red and green colors, represented the colocalization of PSD-95 and α CaMKII.

In the combined images, the bright dots representing neuronal spines were mostly yellow, which strongly suggested that CaMKII and PSD-95 do in fact colocalize at neuronal synapses (FIG. 1C). Red 6G9 staining could be seen along spines and was dense in the cell body as well (FIG. 1B). This observation confirmed previous biochemical findings that showed CaMKII to be a prevalent, cytosolic protein produced in CNS neurons. Frances showed greater background staining, especially evident from no-primary control images. We also observed staining for PSD-95 in what appeared to be glial cells (data not shown). This led us to suspect that PSD-95 might be expressed in glial cells.

Montage of Double-Staining Single Images

Viewing single overlay images gave only relatively local information about single neurons. To get a sense of the colocalization of proteins throughout a cell culture, a collection of many images was needed to establish consistent finding. Thus, overlay images of double-staining with 6G9 and Frances were taken from regions adjacent to each other on the coverslip. A montage image overlooking the entire composite region was then constructed from the single images. From the result of these montages (FIG. 2), we were able to identify

three types of cells represented in the cultures. The majority of neurons stained for both PSD-95 and α CaMKII. However, there appeared to be a small population of neurons that was stained only for PSD-95

(see the green, polar-shaped neurons in FIG. 2). A third class was the glial cells. It seemed that glial cells were stained only by Frances, but not by 6G9.

We quantified the numbers of each cell type. Shown in Table 1, approximately half of the cells in the cultures were neurons, while the other half were glial cells. These data were collected from a representative region of approximately 0.57% of a coverslip total area.

Discussion and Conclusion

By immunocytochemical techniques, we have shown that two proteins in the PSD fraction, α CaMKII and PSD-95, are colocalized at neuronal synapses in hippocampal cell cultures. There also exists a small population of neurons that appears to be stained only for PSD-95. The body shape of this small group of neurons is unusual. They have a bipolar shape, as opposed to the more common radially-shaped neurons. Studies have shown that in CNS cell cultures, two types of neurons co-exist; 80%

release excitatory signals, and 20% release inhibitory signals and have a bipolar shape⁸. We suspect that the small group of neurons that stained only for PSD-95 is from this second class of inhibitory neurons. Further studies will be performed to examine that hypothesis.

We also found that α CaMKII is stained only in neurons and not in glial cells. In contrast, PSD-95 is stained in both neurons and glial cells. In previous experiments performed utilizing Frances, which stains for PSD-95, this observation of glial staining had never been made. Furthermore, the glial staining varied depending on the purification batch of Frances we used. Thus, we suspect that this glial staining of PSD-95 by Frances might be an artifact due to variations in the antibody fractions when Frances was prepared. There may be antibodies to unknown glial proteins present in the Frances solution that lead to variable staining of glia. Additional studies will be done to examine this speculation.

References

1. Kennedy, M. B., "Regulation of Synaptic Transmission in the Central Nervous System: Long-Term Potentiation," *Cell*, Vol. 59, 777-789, 1989.
2. Kennedy, M. B., "The Postsynaptic Density," *Current Opinion in Neurobiology*, Vol. 3, 732-737, 1993.
3. Patton, B. L., Molloy, S. S., Kennedy, M. B., "Autophosphorylation of Type II CaM Kinase in Hippocampal Neurons: Localization of Phospho and Dephosphokinase with Complementary Phosphorylation Site-Specific Antibodies," *Molecular Biology of the Cell*, Vol. 4, 159-172, 1993.
4. Cho, K.-O., Hunt, C. A., Kennedy, M. B., "The Rat Brain Postsynaptic Density Fraction Contains a Homology of the Drosophila Discs-Large Tumor Suppressor Protein," *Neuron*, Vol. 9, 929-942, 1992.
5. Moon, I. S., Apperson, M. L., Kennedy, M. B., "The Major Tyrosine-phosphorylated Protein in the Postsynaptic Density Fraction is N-methyl-D-aspartate Receptor Subunit 2B," *Proc. Natl. Acad. Sci. USA*, Vol. 91, 3954-3958, 1994.
6. Kornau, H.-C., Schenker, L. T., Kennedy, M. B., Seeburg, P. H., "Domain Interaction Between NMDA Receptor Subunits and the Postsynaptic Density Protein PSD-95," *Science*, Vol. 269, 1995.
7. Nicolls, J. G., Martin, A. R., Wallace, B. G., *From Neuron to Brain*, 146, 1992.
8. Benson, D. L., Watkins, F. H., Steward, O., Banker, G., "Characterization of GABAergic Neurons in Hippocampal Cell Cultures," *Journal of Neurocytology*, Vol. 23, 279-295, 1994.

The Expression and Functional Analysis of Mammalian Olfactory Receptor

Hoai-Ky Vu Ho*, Yinong Zhang, Henry A. Lester, & Kai G. Zinn

* University of Oregon

Introduction

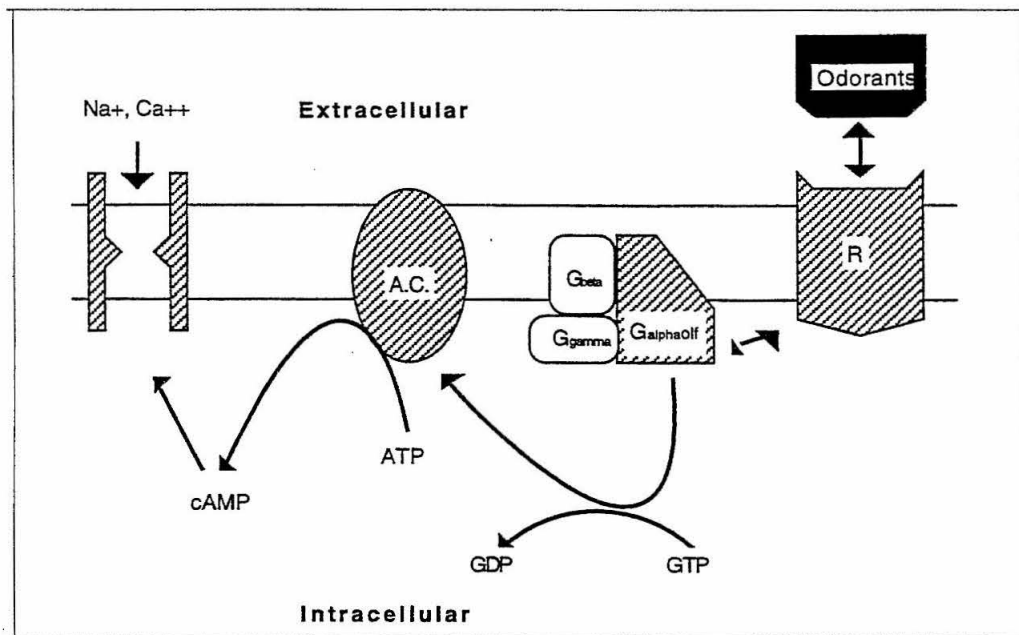
Sensory transduction transforms external physical stimuli into internal biochemical or electrical signals that can be interpreted by the brain. The mammalian olfactory system can recognize and differentiate thousands of odorants that exist in the environment. One mechanism of olfactory signal transduction involves a rapid and transient increase in intracellular cAMP via the typical G-protein coupled receptor activation cascade. This cascade begins with odorant interaction with a 7-transmembrane helix receptor which in turn stimulates activation of a G alpha s-like G-protein called Golf. Finally the activated G-protein stimulates adenylyl cyclase to produce cAMP. The resulting increase in the intracellular cAMP opens cyclic nucleotide-

The expression and cellular localization of a cloned rat olfactory receptor R1 was studied with immunofluorescent microscopy in *Xenopus* oocytes. Three days after mRNA injection myc-tagged R1 receptors were efficiently expressed on the cell surface detected by antibodies. To assay the function of this receptor, mRNAs for the R1 olfactory receptor along with other components of the olfactory signal transduction pathway, including type III adenylyl cyclase (AC) and G_{olf} were injected into *Xenopus* oocytes. Cystic fibrosis transmembrane regulator (CFTR), an adenosine-3',5'-cyclic monophosphate (cAMP) sensitive Cl^- channel, was used as the reporter protein. More than a dozen odorants have been tested. Preliminary results showed that the R1 receptor seems to be capable of responding to aliphatic aldehydes and heterocycles.

gated cation channels in the cilia and dendrites of olfactory receptor neurons, thereby triggering sensory nerve impulses (FIG. 1)¹⁻¹⁰.

A multigene family encoding a large number of 7-helix receptors expressed in rat olfactory epithelium have been identified¹¹. However, it has not been demonstrated that odorants can activate these receptors. The expression and functional assay of the particular cloned rat olfactory receptor R1 has been studied and reported in this paper. *Xenopus* oocyte is employed for in vitro studies of this receptor because it allows both the immunohistochemical staining and electrophysiological two-electrode voltage-clamp recording¹².

FIG. 1. A Schematic Model for the Mechanism of Odorant Signal Transduction



Abbreviations used in this paper: CFTR, cystic fibrosis transmembrane regulator; R, olfactory receptor; AC, type III adenylyl cyclase; G_{olf} , a $G_{\alpha s}$ -like G-protein in the olfactory signal transduction pathway; cAMP, an adenosine-3',5'-cyclic monophosphate; GIRK, G-protein activated inward rectifying K^+ channel.

Presentation and Discussion of Results

Heterologous Expression of the Cloned Rat Olfactory Receptor R1

The 50-ng myc-tagged mRNA encoding the receptor R1 was injected into *Xenopus* oocytes. In order for the receptor R1 to be able to function, it has to be successfully assembled onto the cell surface membrane. The expression and cellular localization of a cloned rat olfactory

receptor R1 was studied with immunofluorescent microscopy in *Xenopus* oocytes (FIG. 2). This receptor was found to be efficiently expressed and inserted into the oocyte surface membrane as indicated with a rim of bright staining. As a positive control, the G-protein activated inward rectifying K⁺ channel (GIRK) protein was also expressed. This protein had been shown to be successfully assembled onto the oocyte surface membrane¹³.

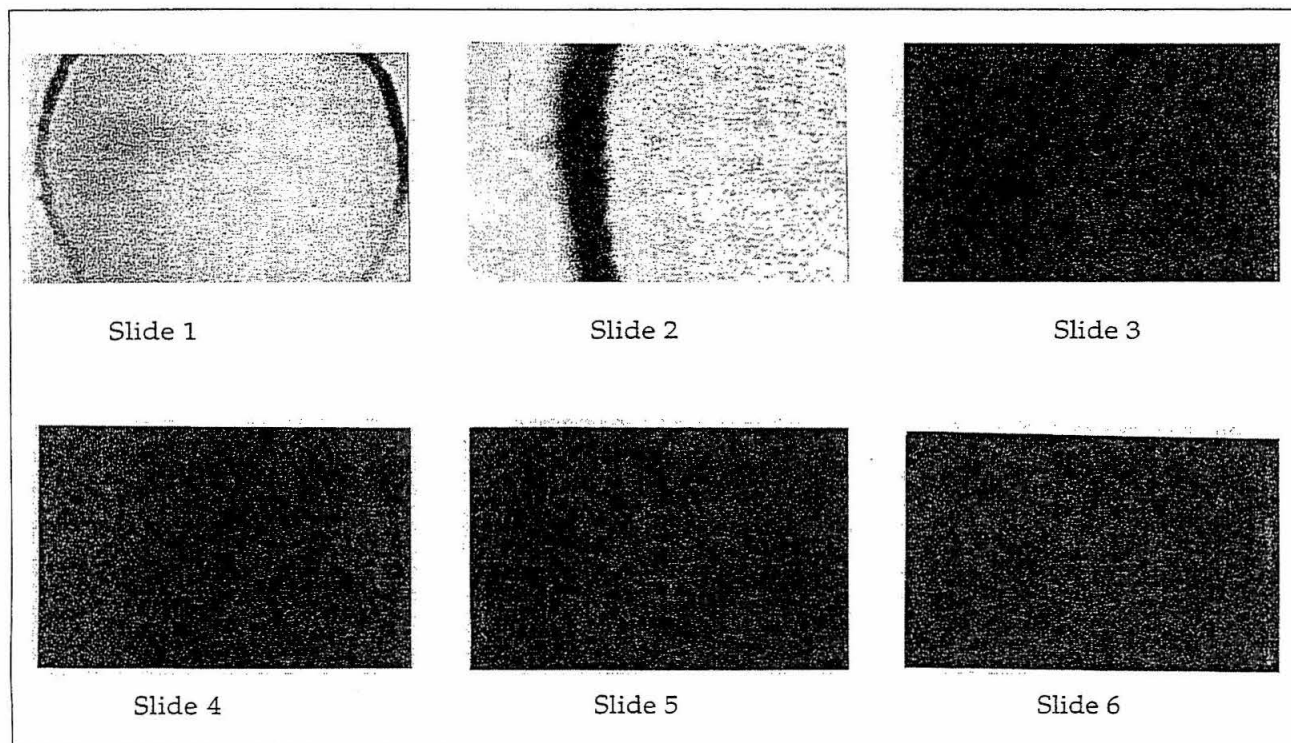


FIG. 2. Heterologous expression of the cloned rat olfactory receptor R1 in *Xenopus* oocytes

Slide 1: A bright field 10x image of a 20 micron thick oocyte cross-section. The inner area is the oocyte cytoplasm. The upper dark-pigmented half is the animal pole whereas the lower light-pigmented the vegetal pole.

Slide 2: A bright field 60x image of a selected oocyte surface membrane segment from the animal pole indicated by the dark-pigmented layer. The region on the right is the oocyte cytoplasm.

Slide 3: A segment of an oocyte uninjected with GIRK mRNA but stained with GIRK antibody. As expected, no K⁺ channels were expressed onto the oocyte surface membrane, and therefore, no antibody binding is observed, indicated by the absence of the bright rim surrounding the oocyte surface.

Slide 4: A segment of an oocyte injected with GIRK mRNA and stained with GIRK antibody. The presence of the bright

rim around the section indicates the K⁺ channel protein was successfully expressed onto the oocyte surface membrane. This result indicates the antibody staining procedure was properly followed and worked well. The dark-pigmented band between the peripheral bright rim on the left and the inner cytoplasm on the right suggests that this oocyte segment is derived from the animal pole.

Slide 5: A segment of an oocyte uninjected with the myc-tagged olfactory receptor R1 mRNA (a negative control). When the oocyte is stained with the myc-tag antibody, no bright rim on the surface is observed as expected.

Slide 6: A segment of an oocyte injected with the myc-tagged olfactory receptor R1 mRNA. When stained with the myc-tag antibody, the oocyte shows a bright layer on its surface, indicating the myc-tagged R1 has been successfully expressed onto the membrane. No dark-pigmented band is present between the peripheral bright rim and the inner cytoplasm, suggesting that this oocyte segment is derived from the vegetal pole.

Functional assay of expressed olfactory receptors

A sensitive electrophysiological assay in *Xenopus* oocytes using the CFTR Cl⁻ channel as a reporter was employed to characterize the expressed rat olfactory receptor R1 in terms of ligand-receptor specificity. In the *Xenopus* oocyte expression system, mRNAs for the olfactory receptor R1 along with other components of the olfactory signal transduction pathway, including type III adenylyl cyclase and Golf, were injected 16ng each. CFTR, a cAMP sensitive Cl⁻ channel, was used as the reporter protein. Upon the binding of odorant molecules, activated olfactory receptor R1 causes the elevation of cAMP through Golf-protein-mediated activation of adenylyl cyclase. The elevated cAMP can then activate a protein kinase, which in turn phosphorylates and opens the CFTR Cl⁻ channel (FIG. 3).

More than a dozen odorants have been tested. Preliminary results showed that the R1 receptor seems to be capable of responding to aliphatic aldehydes and heterocycles. Previous studies have shown the receptor R1 is also capable of responding to lactones and ketones (Y. Uezono, Y. Zhang, unpublished data).

Conclusions

1. The olfactory receptor R1 is successfully assembled onto the cell surface membrane when heterologously expressed in *Xenopus* oocytes.
2. Odorants can activate receptor R1 and generate electrical signals.
3. Receptor R1 is capable of interacting with a group of structurally different odorants.

Acknowledgements

I would like to thank Drs. Kai G. Zinn and Yinong Zhang deeply for their helpful discussions and generous support in making this research project and report possible.

This work was supported by Howard Hughes Medical Institute grant and sponsored by Drs. Kai G. Zinn and Henry A. Lester, California Institute of Technology.

References

1. Reed, R. R., "Signaling Pathways in Odorant Detection," *Neuron*, Vol. 8, 205-209, 1992.
2. Lancet, D. and Benarie, N., "Olfactory Receptors," *Current Biology*, Vol. 3 (10), 668-674, 1993.
3. Nakamura, T., et al., "A Cyclic Nucleotide-gated Conductance in Olfactory Receptor Cilia," *Nature*, Vol. 325, 342-344, 1987.
4. Kurahashi, T., "The Response Induced by Intracellular Cyclic AMP in Isolated Olfactory Receptor Cells of the Newt," *J. Physiol.*, Vol. 430, 355-371, 1990.
5. Firestein, S., et al., "Activation of the Sensory Current in Salamander Olfactory Receptor Neurons Depends on a G-protein-mediated cAMP Second Messenger System," *Neuron*, Vol. 6, 825-835, 1991.
6. Zufall, F., et al., "Analysis of Single Cyclic-nucleotide Gated Channels in Olfactory Receptor Cells," *J.*

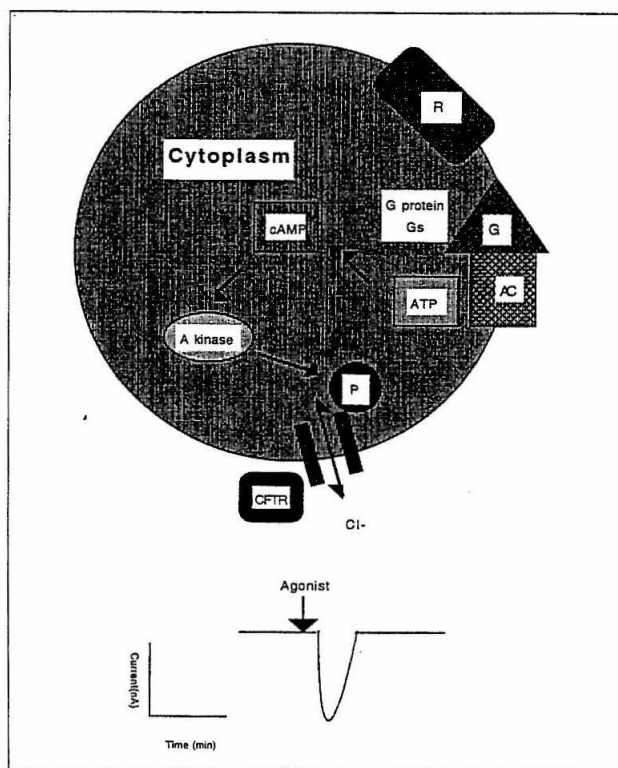


FIG. 3. Seven-helix receptors that couple to the adenylyl cyclase pathway in *Xenopus* oocytes

Neurosci., Vol. 11, 3573-3580, 1991.

7. Frings, S., et al., "Properties of Cyclic Nucleotide-gated Channels Mediating Olfactory Transduction. Activation, Selectivity, and Blockage," *J. Gen. Physiol.*, Vol. 100, 45-67, 1992.
8. Kleene, S. J., "Origin of the Chloride Current in Olfactory Transduction," *Neuron*, Vol. 11, 123-132, 1993.
9. Kurahashi, T., et al., "Coexistence of Cationic and Chloride Components in Odorant-induced Current of Vertebrate Olfactory Receptor Cells," *Nature*, Vol. 363, 71-74, 1993.
10. Lowe, G., et al., "Nonlinear Amplification by Calcium-dependent Chloride Channels in Olfactory Receptor Cells," *Nature*, Vol. 366, 283-286, 1993.
11. Buck, L., et al., "A Novel Multigene Family May Encode Odorant Receptors: a Molecular Basis for Odor Recognition," *Cell*, Vol. 65, 175-187, 1991.
12. Uezono, Y., et al., "Receptors that Couple to Two Classes of G-proteins Increase cAMP and Activate CFTR Expressed in *Xenopus* Oocytes," *Receptors and Channels*, Vol. 1, 233-241, 1993.
13. Bausch, S., et al., "Immunocytochemical Localization of Delta-opioid Receptors in Mouse Brain," *J. Chem. Neuroanatomy*, Vol. 8 (3), 175-189, 1995.

Colocalization of Postsynaptic Density Proteins α CaMKII and NR2B in Dissociated Hippocampal Neurons

Lin Z. Jia and Mary B. Kennedy

The postsynaptic density (PSD) is a prominent synaptic organelle of the brain. Proteins in the PSD participate in signal transduction interactions that contribute to synaptic plasticity and long term potentiation (LTP), both of which may be important for learning and memory formation. Immunocytochemical double-labeling experiments of two of these proteins, the α subunit of the Ca^{2+} /calmodulin-dependent protein kinase II (CaMKII) and the 2B subunit of the NMDA-type glutamate receptor (NR2B), produced evidence for their colocalization within the PSD. Both proteins were present along dendrites and highly concentrated at most synapses. These results help indicate the nature of interaction between α CaMKII and NR2B and their subsequent contribution to synaptic plasticity and LTP.

Introduction

In the central nervous system, the brain sends and receives information with precision and speed. At the molecular level, this job is carried out by special chemical messengers at regions called synapses in the brain. It is proposed that learning and memory may result from the repeated signaling of these chemical messengers and their interactions with proteins involved in signal transduction pathways. As more messengers are sent at a synapse, these proteins respond, and the synapses become stronger. In addition, as synapses are activated more frequently, the stronger response of the synapse may last for a longer time. It is believed that the capability of synapses to strengthen

with previous triggering, which is termed synaptic plasticity, leads to the encoding of memory. It is also believed that the sustained increase in synaptic response, which is termed long term potentiation (LTP), is essential for learning.

Under the electron microscope, one can see a thick and dense region in the cytosol underneath the postsynaptic membranes termed the postsynaptic density (PSD). Through a process of purification of synaptic membranes, extraction with 0.5% Triton X-100 detergent, further purification by centrifugation, and isolation of individual proteins from the PSD on SDS-PAGE gels, a number of PSD proteins have been identified. Dr. Kennedy's lab has isolated, sequenced, and prepared antibodies against four PSD proteins – α CaMKII¹ (Ca^{2+} /calmodulin-dependent protein kinase II), NR2B² (a subunit of the NMDA-type glutamate receptor), PSD-95, and Densin-180.

Based on the location of the PSD and its importance in relation to signal pathways in the brain, several functions have been proposed for these proteins. They may control adhesion between presynaptic and postsynaptic membranes and they may also regulate neurotransmitter receptors through signal transduction complexes that respond to activation of these receptors³.

The quantity of these proteins in the PSD indicates that they may play an important role at the synaptic junction and perhaps also in subsequent signal transduction pathways. However, when these proteins were purified from the PSD, they were not purified from one PSD. The PSD fraction was a pool of PSDs from different kinds of synapses in the brain. To further study and characterize these proteins, we are interested in the location of these proteins within PSDs from different kinds of synapses.

In particular, biochemical studies have indicated a possible transduction pathway between α CaMKII (a protein kinase present throughout the neural cytosol as well as in the PSDs which senses calcium signals that trigger LTP induction) and NR2B (the NMDA-type glutamate receptor subunit 2B that is a component of ion channels which regulate the flow of calcium ions into postsynaptic membranes). The goal of this project was to study whether these two proteins are present at the same PSDs and to observe whether they are colocalized with each other and consequently become optimally positioned in an effective signal pathway.

Procedures

Localization of α CaMKII and NR2B was carried out by immunocytochemical double-labeling experiments. Dissociated hippocampal neurons were grown on cover slips. The cultures were rinsed with Dulbecco's Phosphate Buffer Saline (D-PBS)⁴, fixed in cold methanol (-20°C) for 20 minutes, rinsed in D-PBS, then pre-incubated in preblocking buffer⁵ for 1 hour. For double-staining, cultures were incubated overnight at 4°C with mouse anti- α CaMKII (6G9; 1/500) and a rabbit serum against NR2B (Xandria; 1/500). The cells were then washed with preblocking buffer and incubated for 1 hour with a mixture of fluorescent probes, goat anti-mouse IgG conjugated to Cy3 (α CaMKII) and goat anti-rabbit IgG conjugated to Fluorescein (NR2B), each at 1/100 dilution. The cultures were washed, cover-slipped and viewed in a Zeiss LSM 310 laser-scan confocal microscope.

Cy3 was excited by the scanning laser at 543 nm and Fluorescein was excited at 488 nm. Their emissions at 590 nm and 500 nm produced the colors red and green respectively. The images were sent to a computer monitor and stored on a computer disk.

α CaMKII and NR2B localization was first studied individually to detect their presence at synapses. Corresponding sets of double-labeled images were then combined with the computer program Photoshop. Bright yellow staining, the result of combining red with green, indicated colocalization of α CaMKII and NR2B in the neurons.

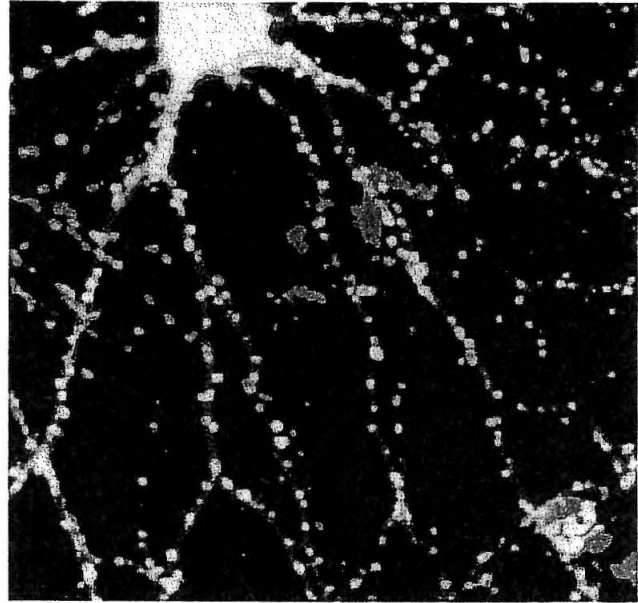


FIG. 2. Colocalization of α CaMKII and NR2B

FIG. 1. Localization of α CaMKII and NR2B

α CaMKII (FIG. 1A) and NR2B (FIG. 1B) are both highly concentrated at synapses. Combination of the two individual images shows that α CaMKII and NR2B colocalize at most synapses (FIG. 1C).

FIG. 1A. α CaMKII

FIG. 1B NR2B

FIG. 1C. α CaMKII & NR2B



Table 1. Excitation and emission frequencies

Fluorescent	Excitation	Emission	Color
Labeling	Frequency	Frequency	Observed
Cy3	543 nm	590 nm	red
Fluorescein	488 nm	500 nm	green

Results

Dissociated hippocampal neurons were stained with primary and secondary antibodies for α CaMKII (red) and NR2B (green) as described under Procedures. Double-labeled images showed a concentration of each individual protein at synapses. The subsequent combination of corresponding double-labeled images showed evidence for colocalization at most synapses.

Localization of α CaMKII

α CaMKII was concentrated in the synapses and also present in dendrites of neurons. In addition, because of its role as a cytosolic protein as well as a PSD protein, labeling was also apparent in the cell bodies of neurons (FIG. 1A).

Localization of NR2B

NR2B was also concentrated in the synapses but was less evident in dendrites of neurons. In mature neurons, cell bodies were only faintly stained. This supports biochemical evidence that NR2B is principally a synaptic protein and is not known to exist in great concentrations within the cell body (FIG. 1B).

Colocalization of α CaMKII and NR2B

In combined double-labeled images, bright yellow staining at synapses along dendrites indicated colocalization of α CaMKII and NR2B. The higher concentration of cytosolic staining observed for α CaMKII produced a reddish color in the cell bodies of the double-labeled neurons (FIG. 1C, FIG. 2).

Conclusions

Immunocytochemical double-labeling experiments of the α subunit of the Ca^{2+} /calmodulin-dependent protein kinase II (α CaMKII) and the 2B subunit of the NMDA-type glutamate receptor (NR2B) produced evidence for their colocalization within the PSD. Both proteins were present along dendrites and were highly concentrated at most synapses. This result supports biochemical studies that suggest a signal transduction pathway between α CaMKII and NR2B and indicates an effective interaction that positions the proteins to work together to sense changes in the cellular environment.

The special chemical messengers that coordinate signaling and excitation in the brain rely on the individual characteristics and properties of these postsynaptic density proteins to relay messages to the cells around them. Thus it is the subsequent signal transduction pathways carried out by the postsynaptic density proteins that lead to morphological and physiological changes which bring about the strengthening in synapses (synaptic plasticity) and the sustained increase in synaptic response (LTP). Further work can be carried out to determine if the other proteins in the PSD, PSD-95 and Densin, will also colocalize with α CaMKII and NR2B. These results would provide a wealth of information concerning the nature of interactions between PSD proteins and their contribution to synaptic plasticity and LTP. This project is part of the ongoing research in Professor Kennedy's laboratory to study signal transduction in the brain with the final hope of elucidating mechanisms of memory and learning in humans.

Acknowledgments

I thank Leslie Schenker for her technical help and advice. This work was supported by Mary B. Kennedy and the Summer Undergraduate Research Fellowships (SURF) program at Caltech.

References and Notes

1. Kennedy, M. B., Bennett, M. K., Erondy, N. E., "Biochemical and Immunochemical Evidence that the 'Major Postsynaptic Density Protein' is a Subunit of a Calmodulin-dependent Protein Kinase," *Proc. Natl. Acad. Sci. USA*, Vol. 80, 7357-7361, 1983.
2. Moon, I. S., Apperson, M. L., Kennedy, M. B., "The Major Tyrosine-Phosphorylated Protein in the Postsynaptic Density Fraction is N-methyl-D-aspartate Receptor Subunit 2B," *Proc. Natl. Acad. Sci. USA*, Vol. 91, 3954-3958, 1994.
3. Kennedy, M. B., "The Postsynaptic Density," *Current Opinion in Neurobiology*, Vol. 3, 732-737, 1993.
4. Dulbecco's Phosphate Buffer Saline consists of 0.1gm/L CaCl_2 , 0.2gm/L KCl , 0.2gm/L KH_2PO_4 , 0.1gm/L $\text{MgCl}_2 \cdot 6\text{H}_2\text{O}$, 8.0gm/L NaCl , and 2.16gm/L $\text{Na}_2\text{HPO}_4 \cdot 7\text{H}_2\text{O}$.
5. Preblocking buffer consists of 0.05% Triton X-100 and 5% normal goat serum in h-PBS (20mM Na_2PO_4 , pH7.4, 450mM NaCl).

Bidding for Computer Time

Minneola P. Ingersoll*, David Krider^K,
Andrew Ingersoll^K, & Scott E. Page^K

* Stanford University

^K First Quadrant, 800 E. Colorado Boulevard,
Suite 900, Pasadena, CA, 91101

First Quadrant, an institutional money management firm, analyzes data using a network of 16 computers. When two or more users run jobs simultaneously, the processors become congested, and work is slowed. To make this system more efficient, I designed a priority system based upon a job's urgency and a user's opportunity cost of waiting. Users purchase priority with fiat money to move a job faster through the system. In this manner, each user is able to complete his/her most urgent jobs rapidly. To test this approach, I wrote a simulation in C, which shows that even under varied initial conditions, the new system is fair to everyone involved.

Introduction

A network of less powerful computers can simulate the capabilities of a supercomputer. Network systems are often characterized by ample capacity on average, but insufficient capacity during peak periods. Demand is not constant, but it is possible to make the demand distribution more efficient. The present study meets the goals of the individual as well as the goals of the group as a whole. First Quadrant was the model for my work.

The problem arises when two or more users try to run jobs simultaneously. This creates congestion at the processors. Every additional user contributes to the congestion. When making decisions about when to run their jobs users act according to their own knowledge and interests, but fail to take into account the delays they impose on others. Computer time is being treated as a public good. By making it free to everyone, there is no incentive for users not to use the system during peak load periods¹.

My study tested the hypothesis that a market-like system in which users purchase priority with fiat money will expedite completion of a user's most urgent jobs. I developed a bidding algorithm to assign priority and introduced a method to allocate computer processing time randomly, according to each user's normalized priority number. Using a computer simulation I determined the efficacy of this system under varied conditions.

Methods

First Quadrant operates a network of sixteen computer processors that work in parallel to simulate a more powerful mainframe. Every job includes thousands of much smaller individual tasks. When each user enters the system, his/her first sixteen tasks are distributed one to each processor. If a task arrives at a processor that is already in use, the new task will enter a first-in first-out queue to obtain service. When a processor finishes a task, the system sends another one of that user's tasks to that processor. Each user always has a task in line at every processor, but never more than one.

Fiat Money

The process in use at First Quadrant works best when the value of fast service is the same for all users. Unfortunately, some jobs are more urgent than others, not all tasks take the same amount of time to complete, and processors operate at different speeds. To quantify the cost of delay, or opportunity cost, users should be penalized for the delays they impose on others. This is the principle of causality -- he who causes cost should be charged². My approach uses a dynamic pricing structure to lower rates during idle periods. When submitting jobs, users must have some knowledge of the current system demand³.

I introduced fiat money (non-legal tender) that can be used to purchase priority. At the beginning of every month (or other time horizon) a user accrues a certain amount of currency based upon factors including: the number of tasks they have to execute, the importance of these tasks, and the opportunity cost of delays to the particular user. Many of these criteria, such as the importance of a task, are not easily quantified. To award each user his/her proper quota of fiat money, I suggest that each department, or area of the firm, makes allocations to the users under their jurisdiction. This allotment can be used to purchase computer time for the next two months.

Program Design

I wrote a program, RAD (Resource Allocation Design), to evaluate different bidding strategies. By studying my proposed algorithms actually in use I was better able to guide their design, and reformulate my notions of performance in response to observation. The first change I made was to allocate tasks using the system as a whole, rather than allowing each processor to operate independently. The system maintains a single queue that services all of the processors.

At First Quadrant, jobs are set up so that on identical processors, all tasks from one user will take the same amount of time to execute. However, task lengths will vary from user to user. Additionally, processors are not equally powerful. RAD uses the product of the user's expected task length and the processor's expected speed to estimate the amount of time a single task will take to execute at a particular processor.

All of a user's thousands of tasks must be finished before a job is complete. Before being processed, each job is divided into generations, groups of hundreds of identical tasks. All of the tasks of a generation must be complete before beginning a new generation. After this process has been repeated for all generations, the job is done, and the time elapsed is recorded. At the end of the simulation, RAD reports the number of jobs completed, the time it took each user to finish, and the amount each paid. RAD reports time units as seconds. This is arbitrary, and could be any discrete, indivisible, integral time unit.

Priority/Payment

My algorithm is simple, and is based on two numbers specified by the user. Before submitting a job the user is told the total of all the bids of the users currently in the system (sumBid). If this number is high the user can choose to wait until a time when there is lower system demand. If the user chooses not to wait, the user is then asked for his/her own maximum bid (userBid). Because it would be unfair to charge a user this amount when it buys faster service than he/she actually requires, a user is also asked to specify a maximum fraction of the system that he/she wants to use (userFraction).

Based upon these two numbers and the immediate state of the system, each task is assigned a priority and payment value:

```
if (userFraction)*(sumBid)<userBid then
    initialPriority = userFraction
    taskPayment = userFraction*sumBid
else
    initialPriority = (userBid/sumBid)
    taskPayment = userBid
```

The sumBid value includes the bid of the user entering the system. When a new job enters the system, sumBid changes and initialPriority and taskPriority are recalculated. It is also necessary to compensate for different task lengths. Rather than charge a user per unit time that he/she uses the system⁴, RAD divides the initialPriority by the task's expected service time, giving larger tasks a lower priority:

```
taskPriority=initialPriority/
    serviceTime
```

Once all priorities have been determined RAD calculates the sum of these priorities. Based upon this sum and a user's own priority value, every user is assigned a percentage of the total system. This percentage can be thought of as a portion of a roulette wheel. When a processor becomes free RAD spins this roulette wheel and services the user in whose region the roulette ball has stopped. This is done internally by RAD using a random number generator.

A user's payment is calculated per task. Every time one of a user's tasks is sent to a processor the user's total payment is incremented by the taskPayment.

Results

It is possible to run RAD under random conditions, or under identical and repeatable conditions. Figures 1 through 4 demonstrate that under non-random conditions, RAD repeatedly generates results to support our hypothesis that by purchasing priority, users will be able to more quickly complete their most important jobs.

Figures 1 and 2 display the results of a test run with three users who submit jobs to the system at the same time. All three users requested 50% of the system, and I tested the effects of changing the bid of the third user. In this example the other users each bid 20. The first two users had an infinite number of identical tasks to execute. The third user was relatively small (200 tasks). The program ran until all of user three's tasks were finished. As the third user's bid changed I recorded the amount of time it took him/her to finish. The straight line at time=50 is the amount of time that it would take the system to finish user three's 200 tasks if there were no other users. Figure 2 records the third user's payment.

Figures 3 and 4 display the same experiment when all three users have requested 25% of the system instead of 50%. Again, the first two users have each bid 20. When complex processes are involved and models are developed, these models will necessarily be simplifications of the real world. Running the program with nearly identical users makes it easier to compare experimental results with hypothetical results, but we need to be more careful in our interpretation. We notice in Figures 1 and 3 that as the user's bid approaches zero the completion time approaches infinity. In this system the other two users can be considered infinite and will always have non-zero bids. While this is true, a bid of zero will never be served.

Figure 1

From my algorithm, as long as (userFraction *sumBid) > userBid the user will be constrained by the userBid rather than by the userFraction. Any point where one of the users' limiting numbers changes is a break point. At these points the method of calculating both the priority and the payment will change. The graphs of both time and payment will be affected at these points.

In Figures 1 and 2 there is only one break point. Either solving algebraically or reading from the graphs, it is clear that when the other users have each bid 20 the break point will be at userBid=40. There is only one break point because user three changes only once from being constrained by his/her userBid to his/her userFraction. Additionally, the other two users are always constrained by their userBid.

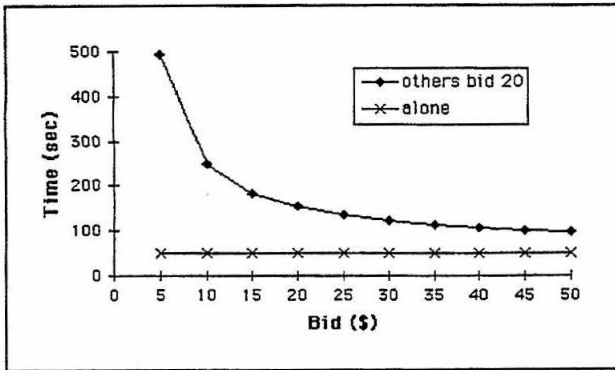


FIG. 1. User's bid versus time to complete all the user's tasks when all three users request 50% of the system

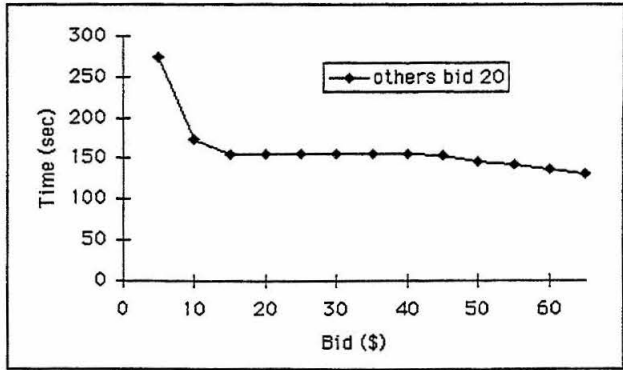


FIG. 3. User's bid versus time to complete all the user's tasks when all three users request 25% of the system

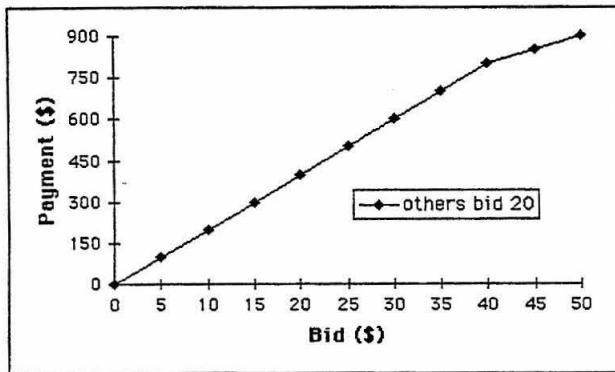


FIG. 2. User's bid versus his/her total payment after leaving the system. All three users requested 50% of the system.

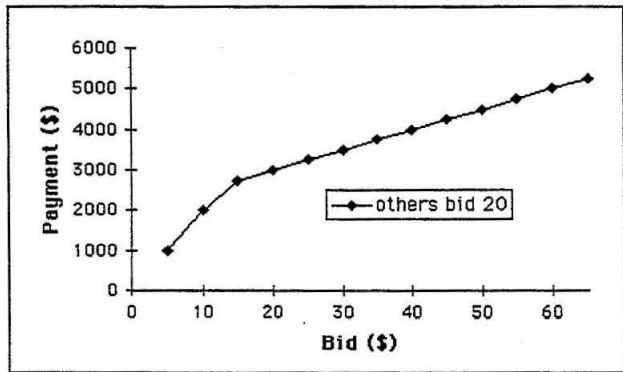


FIG. 4. User's bid versus his/her total payment after leaving the system. All three users requested 25% of the system.

Before the break point the graph is

$$\begin{aligned} \text{time} &= \text{minWait} / (1 - \text{sumOther} / \text{sumBid}) \\ &= (\text{minWait} * \text{sumBid}) / (\text{sumBid} - \text{sumOther}) \\ &= (\text{minWait} * (\text{sumOther} + \text{userBid})) / \text{userBid} \\ \text{time} &= (\text{minWait} * \text{sumOther}) / \text{userBid} + \text{minWait} \end{aligned}$$

After the break point the graph is

$$\begin{aligned} \text{time} &= (\text{minWait} (2 * \text{userBid} + \text{userFraction} * \text{sumBid})) / (\text{userFraction} * \text{sumBid}) \\ &= \text{minWait} (\text{sumOther} / (\text{userFraction} * \text{sumBid})) + \text{minWait} \\ \text{time} &= (\text{minWait} * \text{sumOther}) / ((\text{sumOther} + \text{userBid}) * \text{userFraction}) + \text{minWait} \end{aligned}$$

Here the minWait is 50, the sumOther is the sumBid for the other users in the system when user three enters, and the userBid is user three's bid. These graphs are asymptotic to $\text{time} = 50$ and inversely related to the userBid. We expect an asymptote at $\text{time} = 50$ since a job will never take less than 50 seconds to run. Especially in the second

region, increasing user three's bid by large amounts has little effect on his/her completion time. From the equations we see that this is due to the extra term sumOther in the denominator.

Because we have assumed that all users submit their jobs at the same time, it is easy to compare these results to the results under First Quadrant's current system. Without priorities a user would never complete a job faster than the product of the minimum service time (50) and the number of users (3). Obviously, this is not desirable when a user has a very urgent request.

Figure 2

As a user's bid goes up, his/her payment also goes up. The slope of the payment line will be equal to the number of user three's tasks (in this case 200) until the break point. After the break point it will increase by $\text{userFraction} * \text{numberTasks}$ (in this case 100).

If the other users' bids were half their current value the numbers along the x axis would be half as large. This means it costs more to reach the break point when the sumBid is large. Users will be forced to pay the most when system demand is already high.

Figure 3

Instead of a constantly decreasing function as in Figure 1, Figure 3 plateaus between a bid of 15 and 40. In the first region user three is constrained by his/her maximum bid and the other users are constrained by their userFraction. Increasing user three's bid lowers the completion time. In the plateau region, all three users are constrained by their maximum fraction (25%). This is why when raising his/her own bid (and thus the sumBid for the entire system) user three sees no reduction in completion time. It is a bidding war where the other users are also being forced to pay more. Finally, the other users are unwilling to pay more because they have reached their own maximum bid. When this happens, user three's time again decreases.

Algebraically, we discover two break points at $40/3$ and at 40. Since my experiment only recorded bid increments of 5, it appears that there are four distinct regions with different slopes, when really there are only three. The plateau region at first appears unfair to user three, but it helps to recall the simplifying assumptions we made earlier. If all the users were not identical then they would reach their maximum bid at different times and the plateau would be shorter lived or less dramatic.

Figure 4

The payment is independent of the behavior of the other users, so the only break point is at $40/3$. Before this point the slope will be equal to the number of tasks, and will be the numberTasks*userFraction after this point (same as Figure 2).

Discussion

Fiat Money

Service delays are frequently ignored or their impact is underestimated. Fiat money makes delays tangible, improves feedback, and provides incentive. The use of fiat money in a distributed system has proved effective in similar applications. It falls into the general category of a market price system. "Market price systems constitute a well-understood class of mechanisms that under certain conditions provide effective decentralization of decision making with minimal communication overhead."⁵ The use of pricing for regulating the size of queues was first studied by Naor⁶. His model was generalized by Edelson and Hildebrand⁷ and Mendelson and Yechiali⁸ among others. The ordering system I implemented assures that tasks will be executed in descending order of importance. Decentralizing the ordering process is better than allowing the decision making to reside with a system administrator who is not fully informed about each user's costs and project merits. The structure of the system may be common knowledge, but individual job characteristics are known only to the user. System reliability is improved when responsibility for operation does not reside entirely in one location^{9,10}. For a more in depth look at the advantages of decentralizing priority assignment see Balachandran¹¹.

Decentralizing was also used for the allotment of fiat money to JPL employees to purchase NASA space station resources⁹. Each department developed its own policies for assigning allotments among its constituents. The overlap between the frequency that money is issued and the time that it can be used eliminates end effects that produce unwanted user behavior at the end of a time period. For example, at the end of the month a user might find that he/she has a lot of money left over. Rather than let this money go to waste, the user will bid more for a job than he/she would have bid at the beginning of the time period.

RAD keeps a record of system use versus time of day to keep users informed about trends in demand. My system only requires that a user know one number, the sumBid, when submitting a job. It is simple to record this number and to chart any noticeable trends. Users will then learn from experience and adapt their behavior according to their expectations. This eliminates the obstacle to long term planning that Nielson predicts would occur with a pricing policy that is entirely dynamic and manual¹. If a user were informed of all changes to the system as they occurred, the user would never get anything done because he/she would have to remain on-line to manually change his/her bid. Using an algorithm is much easier for the user.

Another way to achieve the effect of dynamic pricing is to allow users to pay for priority in advance, but to allow users to buy and sell this priority in an aftermarket. This approach was used at JPL, by the planners of the Natural Gas delivery lines⁹, and by the Spawn system designers¹⁰. In the Spawn system, the purchasing of priority is conducted as a second-price auction. This makes less sense for First Quadrant since agents are considered independent and have little interaction among each other.

By introducing a form of currency, First Quadrant will clearly be able to see which departments, or which individuals, are using the most computer time. Looking at leftover salaries or salary shortages, administrators can better allocate in the future.

Program

My strategy improves both performance and user satisfaction. First, treating the system as a whole simplifies the bidding so that a user is bidding for a fraction of the total system rather than specifying different bids for the different processors. Faster processors will end up serving more tasks, but these details can be hidden from the user.

The two numbers, maximum bid and maximum system fraction, give the people at First Quadrant a means to express their value of fast service. For a price, a user will be able to speed up his/her expected completion time. A long, relatively unimportant job will not be allowed to slow down a more urgent job.

Using a random number in the program won't affect our results because the number of tasks that a user needs served will be in the thousands. With this many tasks the Law of Large Numbers will smooth out irregularities

and assure the validity of results. Each one of a user's tasks is very small. Unlike the work of Marchand and Grether^{12,13}, our tasks are small enough that having a preemptive policy, where a new task is allowed to interrupt the task currently being served, is inefficient.

For system planners, the RAD design allows experimentation with changing system parameters. For example, parameters such as the number of available processors can easily be changed to note the effect of changing capacity. Overall, RAD performs its function as a testbed for short term resource allocation strategies, and even gives valuable insight into long term planning. Clearly, introducing fiat money and a priority system is a good strategy for a company with diverse users and diverse user requirements such as First Quadrant.

Acknowledgments

This material is based upon work supported by Caltech's Summer Undergraduate Research Fellowship with thanks to Dr. Scott E. Page, Mr. David Krider, and Dr. Andrew Ingersoll.

References

1. Nielson, N., "Flexible Pricing: An Approach to the Allocation of Computer Resources," *Fall Joint Computer Conference*, 521-531, 1968.
2. Sanjeev, D. and Mendelson, H., "User Delay Costs and Internal Pricing for a Service Facility," *Management Science*, Vol. 36 (12), 1990.
3. Marchand, M. "Priority Pricing with Application to Time Shared Computers," *Fall Joint Computer Conference*, 511-519, 1968.
4. Singer, N. M., "Prices and the Allocation of Computer Time," *Fall Joint Computer Conference*, 493-498, 1968.
5. Wellman, M., "A Market-Oriented Programming Environment and Its Application to Distributed Multicommodity Flow Problems," *Journal of Artificial Intelligence Research*, Vol. 1, 1-23, 1993.
6. Naor, P., "On the Regulation of Queue Size by Leving Tolls," *Econometrica*, Vol. 37 (1), 15-24, 1969.
7. Edelson, N. M. and Hildebrand, D. K., "Congestion Tolls for Poisson Queueing Processes," *Econometrica*, Vol. 43 (1), 81-92, 1975.
8. Mendelson, H. and Yechiali, U., "Controlling the GIM/1 Queue by Conditional Acceptance of Customers," *European Journal of Operations Research*, Vol. 7, 77-85, 1981.
9. Olsen, M. and Porter, D., "Resource Allocation in Complex Systems."
10. Waldspurger, C. A., Hogg, T., Huberman, B. A., Kephart, J. O., Stornetta, W. S., "Spawn: A Distributed Computational Economy," *IEEE Transactions on Software Engineering*, Vol. 18 (2), 1992.
11. Balachandran, K. R., "Purchasing Priorities in Queues," *Management Science*, Vol. 18 (5), 319-326, 1972.
12. Marchand, M. G., "Priority Pricing," *Management Science*, Vol. 20 (7), 1131-1140, 1974.
13. Grether, D. and Porter, D., "Alternative Methods for the Funding and Allocation of JPL Supercomputing Resources," 1995.

Lattice Gas Cellular Automata with Almost Periodic Initial Conditions

Evan Reed

Cellular automata are of significance in supplying simplified approximations to complicated systems like fluids flowing through porous media. In this SURF project, we developed and implemented a fast numerical tool for lattice gas cellular automata. The algorithm³ both stores and performs the cellular automaton rule on data in circle sequences. This results in efficient data storage and the ability to process infinite or periodic configurations without having to map the configuration back to a lattice to perform the rule. The algorithm is implemented and tested on one dimensional automata, Conway's Life, and the HPP lattice gas cellular automaton. Theoretically, we give a precise bound on the growth rate of the number of intervals. This was stated as an unsolved problem by Hof and Knill³.

Introduction

Lattice gas cellular automata are efficient algorithms which allow realistic simulations of fluids. Lattice gas automata are sometimes superior to other methods, especially in situations where the fluid has complex geometric boundary conditions. In three dimensions, storage and CPU time problems become especially important. The method we use here which has its origin in the theory of dynamical systems³ allows us to store and process such large periodic configurations or infinite aperiodic configurations with a finite amount of data. The size of the data used to store the configuration depends on the complexity of the fluid. The method allows the study of fluid in almost periodic media.

Our purpose here is to test the method on a variety of applications in order to determine for which types it is most efficient.

Cellular Automata

A cellular automaton is a local rule performed on a discrete lattice of cells. Each cell has one of a finite set of possible values corresponding to its state. This state could

represent anything, including the direction of flow of a fluid, or the population density of a species. The CA rule is applied to each cell on the lattice, and uses only the states of a local neighborhood of cells as variables.

The Algorithm

Evaluating the CA rule at every cell for each iteration can require a large amount of effort when dealing with large simulations in higher dimensions. The interval method eliminates the need to apply the rule at every cell in the lattice.

Data is stored on an interval configuration which is the union of half open intervals. Associated with each interval is the value, or state, of all cells that fall within that interval. The entire interval is connected at the ends to form a circle configuration. Points that are adjacent on the lattice are separated by an irrational distance α on the circle map. If the rotation vector α is chosen to be rational, we can realize periodic configurations. Higher-dimensional cellular automata can be performed by establishing an additional rotation vector for each dimension.

In this way, the CA rule need only be applied to the boundaries of each individual interval because all cells within the given interval have the same state. It is a way of grouping cells with the same state together to perform the rule on them all at once. The configuration can be stored and operated on in the circle map. No data conversion is necessary to perform CA rule.

A Bound on the Growth Rate of Intervals

An interesting quantity is the *growth rate* of the number of intervals. It is important because it represents the memory needed to store a circle configuration.

Proposition 4.1 *The number of intervals $|\phi^n(J)|$ has a polynomial upper bound depending on the dimension d :*

$$|\phi^n(J)| \leq |F(\phi^n)| \leq |J|,$$

where $|F(\phi^n)| \leq (2rn + 1)^d$ is the number of lattice points in the influence region of the automaton ϕ^n .

Proof. It is enough to show the claim for $n = 1$ since we can replace ϕ by ϕ^n . Let $A = \{a_1, \dots, a_m\}$ with $0 \leq a_1 < a_2 < \dots < a_m < 1$ be the set of boundary points of the partition J . The set of boundary points of the new partition $\phi(J)$ is contained in the set $A + F \oplus \alpha$ which contains maximal $|F(\phi)| \leq |A| = |F(\phi)| \leq |J|$ elements. If ϕ has the radius r , then ϕ^n has a radius $\leq nr$. We also used that $|F| \leq (2r + 1)^d$ because F has to be included in a box $[-r, r]^d$ if the radius is r . \square

So the maximum number of intervals that exist n iterations after there are k intervals with a CA of radius of effect r and dimension d is $k(2rn + 1)^d$.

The Periodic Case

In the periodic case, when α_i are all rational, the interval method can be seen as a method to perform the CA computations in a *compressed way*. Knowing the number of intervals needed during a computation tells us about the compression efficiency of the method.

Given an initial configuration x , how do we choose rational rotation numbers α_i , in order to be able to realize the configuration x with the interval method?

Proposition 5.1 *Assume the largest common divisor of the numbers M_i is 1. If $\alpha_i = 1/M_i$, then there is a bijective relation between the set $J(\alpha_1, \dots, \alpha_d)$ of interval configurations J with boundary points in the set $\{n \in \mathbb{Z} \mid n \equiv 0 \pmod{1}\}$ and the set*

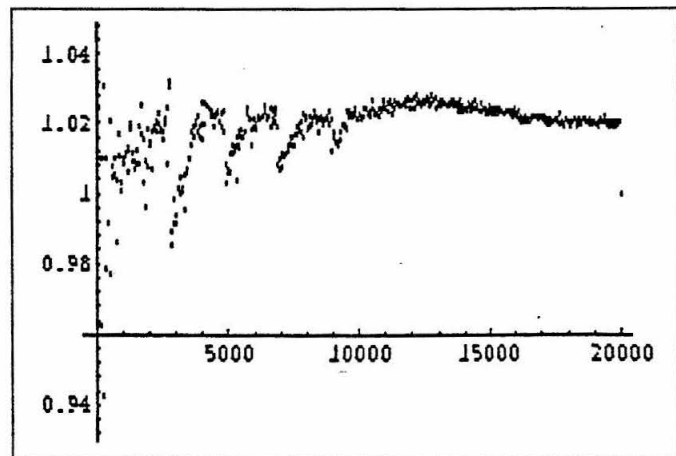
$$X(M_1, \dots, M_d) = \{x \in X \mid x_{n+M_i} = x_n, \forall n \in \mathbb{Z}^d\}.$$

Proof. Fix θ . Every interval configuration $J \in J(\alpha_1, \dots, \alpha_d)$ defines a point in $X(M_1, \dots, M_d)$ by $\psi(J) = x_n = 1_J(\theta + n \in \alpha)$. This map ψ is clearly injective. Since the number of points in $X(M_1, \dots, M_d)$ are both $M_1 M_2 \dots M_d$, the map ψ is also surjective. \square

So if the LCD of $1/\alpha_1$ and $1/\alpha_2$ is 1, then we have a periodic two-dimensional configuration of size α_1 by α_2 .

Assume now the rational rotation vectors α_i have been fixed. How many intervals do we have to store during a run of a cellular automaton? If L is the smallest common multiple of the denominators q_i of the $\alpha_i = p_i/q_i$, then the number of intervals is trivially bounded above by L . However, we expect that the probability of one of the adjacent intervals having the same state is $1/N$. Assuming a scenario of a completely randomized lattice, the ratio of intervals to total number of cells in the simulation will be $(N-1)/N$. The situation can however be much better because some organization can occur. We observed that such organization will improve this compression ratio.

FIG. 1. The one-dimensional automaton ϕ_{18}
Plotted is the ratio of the logarithm of intervals to the logarithm of iterations. The rotation angle was $\alpha = 3^{0.5} - 1$ with initial configuration $J = (0.4, 0.601)$. Only every 100'th value is plotted on this log-log plot.



Results

One-dimensional Cellular Automata

There are 256 one dimensional cellular automata rules with radius one. These are rules that consider the states of only the two nearest neighbors and the cell to which the rule is being applied. Such automata are called *elementary automata*. Typical phase space pictures of these automata are given by Wolfram⁵. Perhaps the most popular of these automata is ϕ_{18} in Wolfram numbering⁴. It has been studied quite extensively because it produces nonlinear behavior in the motion of *kinks*.

We made experiments showing the evolution of the intervals. Occasionally, discontinuities in the behavior of the number of intervals are observed.

Conway's Game of Life

Perhaps the most popular two-dimensional automation is Conway's Life. This is a simple CA in which there are two possible cell states, dead and alive. A living cell dies if there are too few or too many surrounding cells. A dead cell can come to life if surrounded by a certain number of living cells. The CA is designed to mimic a simple biological system.

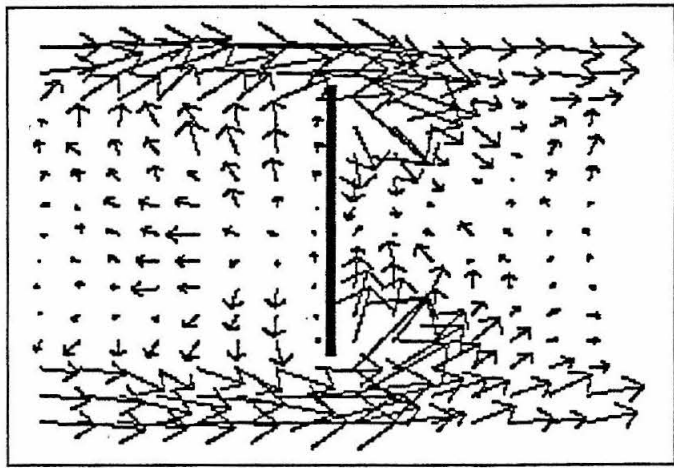
For a completely randomized initial Life simulation with each cell having one of its two possible states, the randomized limit for number of boundary points on the interval is expected to be 1/2 of the maximal possible number of intervals. The actual values in our computations were much lower. This is due to the tendency of Life to die out in large regions and to leave a "desert" with occasional periodic structures of life.

The HPP Lattice Gas Automaton

Lattice gas automata model particles moving on a lattice. They can be used in place of complicated equations to model complex fluid-flow situations, like fluids flowing through a *porous medium* or *immiscible fluids*. The simplest lattice gas model is the HPP model of Hardy, Pazzis, and

FIG. 2. HPP lattice gas automaton

A reflecting object of size 10×400 cells is centered in the middle of a 599×600 periodic lattice. The top and bottom boundaries are reflecting also, so only the right and left sides of the picture are identified. For this simulation, $\alpha = 1/600$, $\beta = 1/599$. There are maximal $600 * 599 = 359400$ intervals. We have a high viscosity (initially, there are about 2 particles per cell). On average, one of these is moving to the right, the other in some other random direction. The vectors represent flow velocity. This particular shot is taken after 1700 iterations. We averaged over a region of size 40×40 and plotted these averaged velocity vectors.



Pomeau^{1,2}. With up to four particles at each cell, there are $N = 2^4 = 16$ possible cell states for such a cellular automaton. For the HPP model, we established a lower interval growth bound. In the HPP CA, n iterations after there are k intervals, there are $k(2n^2 + 2n + 1)$ intervals. This is roughly half of the general two-dimensional bound. An additional cell state can be added to act as a particle reflector. This allows solid objects to be represented in cellular automata simulations.

Conclusions

1. The maximum number of intervals required to represent a cellular automation of dimension d with radius r after n iterations with k initial boundary points is $k(2rn + 1)^d$.
2. In the periodic case, let M^d denote the number of cells in the lattice of a cellular automation with N possible states at each cell. Then the number of intervals on the subshift for a completely randomized configuration is expected to be $M^d(N-1)/N$. This is a heuristic estimate which was confirmed in the experiments.
3. The interval method runs a periodic simulation of life faster. It allows us to process configurations as large as we wish, even lattices which could not be stored in the memory of a given computer.
4. The interval method runs a periodic simulation of the HPP lattice gas cellular automation faster or allows a

configuration larger than the standard method of evaluating cellular automata.

5. The interval method is, in a sense, infinitely effective in evaluating aperiodic situations which naturally occur often in structures like crystals. Traditional cellular automata evaluation can only approximate aperiodic configurations by a periodic situation or by taking artificial boundary conditions.

References

1. Hardy, J., de Pazzis, O., Pomeau, Y., "Molecular Dynamics of a Classical Lattice Gas: Transport Properties and Time Correlation Functions," *Phys. Rev. A*, Vol. 13, 1949-1961, 1976.
2. Hardy, J. and Pomeau, Y., "Thermodynamics and Hydrodynamics for a Modeled Fluid," *J. Math. Phys.*, Vol. 13, 1042-1051, 1972.
3. Hof, A. and Knill, O., "Cellular Automata with Almost Periodic Initial Conditions," *Nonlinearity*, Vol. 8, 477-491, 1995.
4. Wolfram, S., "Statistical Mechanics of Cellular Automata," *Rev. Mod. Phys.*, Vol. 55, 601-644, 1983.
5. Wolfram, S., *Theory and Applications of Cellular Automata*, World Scientific, 1986.

Bell Numbers and k-Trees, and Drawing and Ordering of Trees

Winston Yang and Richard M. Wilson

We summarize some theorems about partitions, Bell numbers, k-trees, and certain kinds of trees.

Bell numbers and k-trees

A partition of a set S is a set of nonempty, disjoint sets (called “parts”) whose union is S . A partition of the empty set is defined to be the empty set. The Bell number B_n is the number of partitions of a set of n elements. The first few Bell numbers, starting with B_0 , are 1, 1, 2, 5, 15, 52, 233. They are named after Eric Temple Bell (1883–1960).

Closely related is the Stirling number of the second kind $S(n, t)$, which is the number of partitions of a set of n elements into t parts; $S(0, 0)$ is defined to be 1, and $S(n, t)$ is defined to be 0 for values of n and t for which the previous two definitions are not applicable. Stirling numbers (of the first and second kind) are named after James Stirling (1692–1770). We have that $B_n = \sum_{t=1, \dots, n} S(n, t)$.

This paper was motivated by counting “columns,” objects considered by Ronald C. Read in a 1962 article “Contributions to the Cell Growth Problem” [R]. We had to count the number of partitions of the set $\{1, \dots, n\}$ with the restriction that each integer i is not in the same part as $i - 1$. We call such partitions “restricted.” We call partitions as defined in the preceding paragraph “unrestricted.”

Theorem 1: The number of restricted partitions of $\{1, \dots, n\}$ is B_{n-1} .

We represent a given partition of the ordered set $\{1, \dots, n\}$ by the ordered set $\{p(1), \dots, p(n)\}$, where $p(i)$ is the part that i is in. We use the following two rules.

1. $p(1) = 1$.
 2. $p(i) \leq 1 + \max(p(1), \dots, p(i - 1))$.
- Rule 2 ensures that if part j is used, then parts $1, \dots, j - 1$ have already been used. For example, one partition of $\{1, 2, 3, 4, 5\}$ is $\{1, 2, 2, 1, 3\}$. There are three parts of the partition: 1 and 4 are in part 1; 2 and 3 are in part 2; 5 is in part 3.

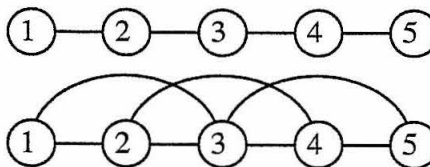
Partitions of vertices of graphs

A partition of a set can be thought of as a “coloring” of the elements in the set; elements have the same colors iff they are in the same part. A proper coloring of a graph is a coloring in which adjacent vertices have different colors. We say that two colorings are isomorphic if one can be obtained from the other by a permutation of the colors.

With this terminology, the problem of counting restricted partitions of $\{1, \dots, n\}$ is a special case of the following problem: For a graph G of a finite number of vertices, what is the number of non-isomorphic proper colorings of G ? Let $nipc(G)$ be the number of non-isomorphic proper colorings of G .

A k -tree of n vertices is defined recursively as follows [ERS]. If $n = k$, then the k -tree is the complete graph K_k . If $n > k$, then the k -tree is formed from a k -tree of $n - 1$ vertices by adding a vertex, and joining it with k edges to k vertices of a complete graph K_k in the existing graph.

Example 1: We show a 1-tree of 5 vertices and a 2-tree of 5 vertices.



Theorem 2: If G is a k -tree of n vertices, then $nipc(G) = B_{n-k}$.

We give a generalization of Theorem 1.

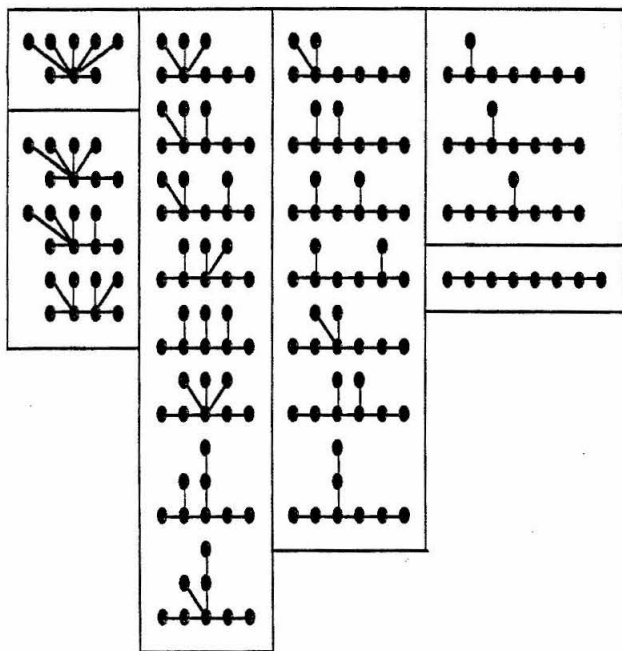
Theorem 3: The number of partitions of $\{1, \dots, n\}$ such that every integer is not in the same part as the previous a distinct integers is B_{n-a} .

Drawing and ordering of trees

A tree is a graph that is connected and has no cycles. Trees have been used in many fields. Kirchhoff discovered trees in 1847 in trying to solve simultaneous linear equations arising from electric circuits. Cayley discovered trees in 1857 while counting saturated hydrocarbons (compounds of the form C_nH_{2n+2}). Tables of the number of trees, and drawings of trees up to 10 vertices, can be found in [H].

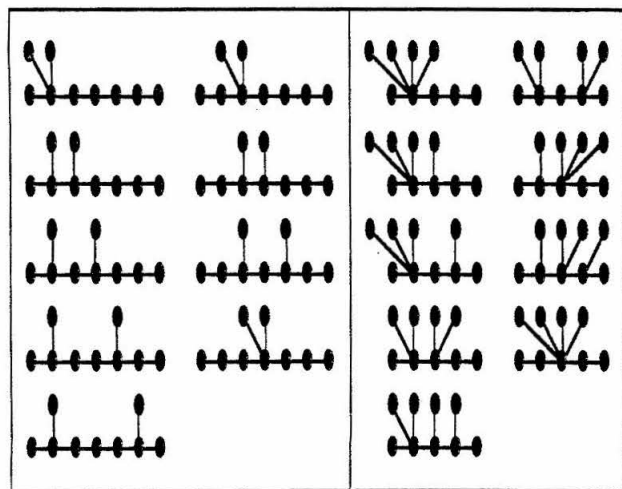
We draw trees using an axial representation; we draw the longest path horizontally [B]. We number the vertices on the longest from the leftmost vertex, starting with 1. An uptree is a subtree that has at least 2 vertices, 1 of which is on the longest path. The height of an uptree is the length of the longest path in the uptree. Therefore a vertex of a tree is on the longest path of the tree iff the vertex has height 0. A linear tree is a tree in which every vertex is on the longest path.

Example 2: We order the 23 trees of 8 vertices, top-down, left-right.



Let $\text{linup}(h_0, \dots, h_m)$ be the number of trees with h_i linear uptrees of height i . "linup" stands for "linear uptrees."

Example 3: We list the 9 trees counted by each of $\text{linup}(7, 2)$ and $\text{linup}(5, 4)$.



We summarize some theorems about $\text{linup}(h_0, h_1)$. Let $\text{choose}(n, k)$ be the number of ways to choose k things from n things, without regard to order.

Theorem 4: $(h_0, h_1) = 1/2 \text{choose}(h_0 + h_1 - 3, h_1) + 1/2 \text{correction}(h_0, h_1)$, where $\text{correction}(h_0, h_1)$ is $\text{choose}((h_0 + h_1 - 3)/2, h_1/2)$ if h_0 is odd and h_1 is even, 0 if h_0 is even and h_1 is odd, $\text{choose}((h_0 + h_1 - 4)/2, h_1/2)$ if h_0 is even and h_1 is even, $\text{choose}((h_0 + h_1 - 4)/2, (h_1 - 1)/2)$ if h_0 is odd and h_1 is odd.

Theorem 5: Let (h_0, h_1) be 1 if $h_1 = 0$ or $h_0 = 3$. Then for $h_1 > 0$ and $h_0 > 3$, $(h_0, h_1) = (h_0 - 1, h_1) + (h_0, h_1 - 1) - \text{correction}(h_0, h_1)$, where $\text{correction}(h_0, h_1)$ is $\text{choose}((h_0 + h_1 - 5)/2, (h_1 - 1)/2)$ if h_0 is even and h_1 is odd, 0 else.

Theorem 6: $\text{linup}(h_0, h_1) = \text{linup}(h_1 + 3, h_0 - 3)$.

Theorem 7: $\text{linup}(h_0, h_1)$ is equal to the number of trees that have a longest path of h_0 vertices and h_1 uptrees, with the restriction that each vertex on the longest path has 0 or 1 uptree.

Acknowledgments

I am especially grateful to the Summer Undergraduate Research Fellowships program (SURF) at Caltech for its support and funding of this research in the summer of 1995; and my adviser Richard M. Wilson for his encouragement, ideas, and readings of drafts of this paper. I would also like to thank Arthur Benjamin, at Harvey Mudd, for communicating another bijection between restricted partitions of $\{1, \dots, n\}$ and unrestricted partitions of $\{1, \dots, n-1\}$; and David M. Jackson, at the University of Waterloo, for communicating another proof that the number of restricted partitions of $\{1, \dots, n\}$ is B_{n-1} .

References

- B = Jean-Pierre Barthélemy and Alain Guénoche, *Trees and Proximity Representations*, John Wiley & Sons, pp.28–31.
 BP = L. W. Beineke and R. E. Pippert, "The Number of Labeled k -Dimensional Trees," *Journal of Combinatorial Theory*, Vol. 6, 1969, pp.200–205.
 ERS = P. Erdős, A. Rényi, and Vera T. Sós (Eds.), *Combinatorial Theory and its Applications III*, Bolyai János Matematikai Társulat, Budapest, Hungary, 1970, pp. 945–946.
 H = Frank Harary, *Graph Theory*, Addison-Wesley Publishing Company, Inc., 1969, pp.231–234.
 IBM = IBM Journal of Research and Development, Vol. 4, 1960, p. 476.
 vLW = Jacobus H. van Lint and Richard M. Wilson, *A Course in Combinatorics*, Cambridge University Press, 1992, pp.20, 105.
 M = J. W. Moon, "The Number of Labeled k -Trees," *Journal of Combinatorial Theory*, Vol. 6, 1969, pp.196–199.
 R = Ronald C. Read, "Contributions to the Cell Growth Problem," *Canadian Journal of Mathematics*, 1962, pp.1–20.
 W = Earl Glen Whitehead, *Enumerative Combinatorics*, New York University, 1972, pp.8–13.

Inflatable Structures Technology

Farouk Hadeed* and Joel C. Sercel

* Yale University

Inflatable structures have widespread applications in the aerospace and planetary exploration fields. The potential uses include communication, power generation, solar thermal propulsion, radiometry, active microwave sensing, very-long-baseline interferometry, microspacecraft, and other interesting applications. This research paper describes an inflatable concept that was constructed and tested at the Jet Propulsion Laboratory in Pasadena, CA. IRIS (Inflatable Reflecting Integrated Structure) was designed as a model of a Power Antenna and displayed at the JPL Open House on July 22-23, 1995. Further tests have been proposed to study many different aspects of inflatables onboard small spacecraft, such as SURFSAT II. The feasibility of this technology for space applications will further be validated by a Space Shuttle mission in April, 1996.

Inflatable Structures. What are they?

We see inflatables everyday - they are manifested in many different applications from tire tubes used in cars and bicycles to giant blimps that rarely go unnoticed in the

sky. But the new kind of inflatables under careful consideration today are different. They have modified characteristics that allow them to do many things quite remarkable for *balloons, which is really what they are!* Applications include communication, power generation, solar thermal propulsion, radiometry, active microwave sensing, very-long-baseline interferometry, microspacecraft, and many other applications in aerospace and planetary research. Inflatable structures have a great many potential uses for space technology programs.

One concept that has shown particular promise is inflatable antennas. In particular, Power Antennas seem set to transform the power generation and telecommunications subsystems of spacecraft for deep space missions.

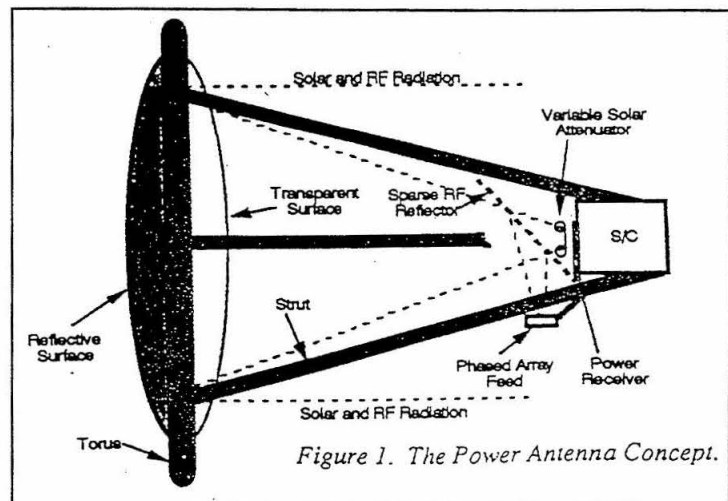
What are Inflatable Antennas?

The concept of filling a non-permeable membrane with a gas and using it as an antenna for communications in space may seem really ludicrous to any reasonable person at first. It sounds like someone saying: "A hot-air balloon is the best ride to Mars!"

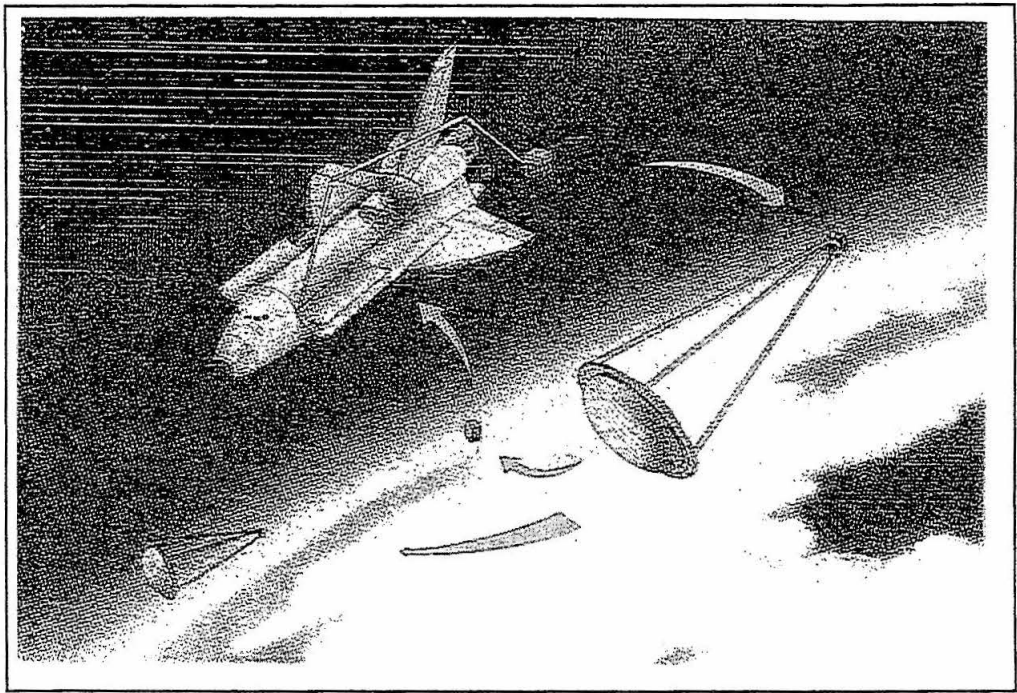
The concept, however, is not all that far-fetched, as the National Aeronautics and Space Administration (NASA) and other small specialized companies, both in the United States and in other countries, have invested in developing an inflatable structure with the properties of a conventional antenna and more. The recognized leader is a company in Tustin, CA named L'Garde, Inc., which has been researching inflatable technologies for many years. The company is now developing a 14-meter diameter inflatable antenna that will test some of the key questions concerning inflatable structures in space.

An inflatable Power Antenna is a parabolic reflector that combines the elements of three major spacecraft subsystems into one piece of hardware. The inflatable reflector functions as

FIG. 1. The power antenna concept



**IN-STEP Inflatable
Antenna Experiment,
Space Shuttle mission,
April 1996**



- 1) a solar concentrator, converting incoming solar rays into electricity for spacecraft power requirements
- 2) a high gain telecommunications antenna for transmitting and receiving data
- 3) a source of heat for thermal control of the spacecraft. (FIG. 1)

This design will offer new ways to reduce power requirements of spacecraft, while providing increased rates of data communication. This assumption is contingent upon the successful demonstration of the concept and its feasibility for use in space.

Part of the plan for validating the Power Antenna concept as an application of inflatable technology is the IN-STEP Inflatable Antenna Experiment, scheduled for a Space Shuttle mission in April, 1996. The goal of this experiment is to validate the principal mechanical performance of the 14-meter diameter inflatable deployable reflector antenna in orbit. From this experiment, which will be administered by NASA, it is likely that the construction of useful inflatable structures and their deployment in space will be verified, and vital characteristic information about reflector surface accuracy will be acquired to compare with analytical models.

In addition to the tertiary purpose of the Power Antenna concept, the advantages of the inflatable antenna (or any inflatable structure in general) over its solid mechanical counterpart are very obvious. Inflatables offer significant reductions in three major factors of crucial importance in space applications:

- 1) Mass. Thin film membrane materials are much lighter than solid rods and fixed dishes, which also tend to be bulky and typically have many points with high probability of failure rates during deployment. Recently, the Galileo mission faced problems due to mechanical (in this case, main antenna) deployment failures, which affected mission objectives.
- 2) Volume. Packaging is an essential ingredient in determining mission objectives, as space is often limited on vehicles that transport spacecraft and materials into orbit. The capacity of the Space Shuttle cargo is what limited the size of the Hubble Space Telescope, for example. The other advantage of inflatables is that they can deploy from very compact packaging sizes to dimensions that can far exceed any imaginable mechanical structure. Inflatable Antennas on the order of 100 meter diameter are envisioned for the future.
- 3) Cost. The cost of building an inflatable antenna is many orders of magnitude less than a conventional mechanical structure. The cost factor becomes more important for larger structures, as the complexity of mechanical structures increases.

What is being done today?

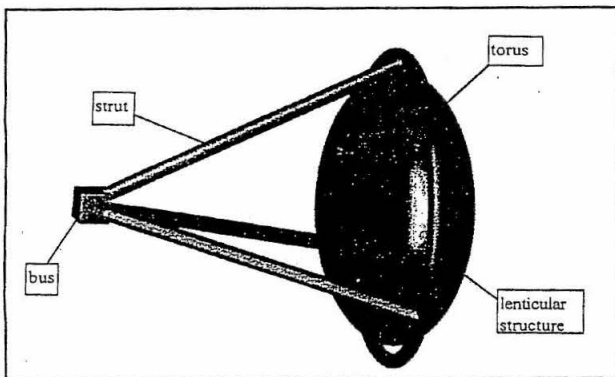
Many of the aforementioned factors are very attractive to NASA, which has recently launched its New Millennium Program to promote a new image of "cheaper, faster, better" than before. The program aims to develop

key technologies for the exploration of space in the 21st century using improved methods of collecting and processing data while carrying out a greater number of quick, focused science experiments. As Manager of the New Millennium Program, the Jet Propulsion Laboratory in Pasadena, CA has been busy identifying new technology concepts to be integrated into the first missions of the 21st century. Among these prospective technologies is inflatable structures.

As part of the effort to develop inflatable Power Antennas, a group of seven New Millennium students from four universities and three countries designed and constructed IRIS (Inflatable Reflecting Integrated Structure), a prototype that demonstrated the feasibility of inflatable technology. It was the first model of the New Millennium Program and was displayed at the annual Open House of the Jet Propulsion Laboratory on July 22-23, 1995.

The IRIS model was made up of four structural sections: a lenticular structure, a torus, three struts, and a base, as shown in Figure 2. The lenticular structure is made of two paraboloids, a reflector and a transparent canopy, mated together by means of an annulus. A torus surrounds the lenticular structure, aligned and attached in the plane of the annulus, primarily to provide support. The torus is connected to three struts which merge at the bus. In designing IRIS, the bus was replaced by a support base for display purposes. The idea, of course, was to have the inflatable structure deploy from the base in a "jack-in-the-box" manner, but the issue of folding and packaging (a very challenging problem for thin membrane materials) was not dealt with in this investigation. One of the most useful outcomes of a correctly packaged inflatable antenna is a systematic deployment sequence that begins with the inflation of the struts, the torus, and finally (at much lower pressures) the lenticular structure. This process is critical and is really the only possible point of failure. After deployment, the system is generally stable and the effects due to temperature gradients and micro meteorite collisions in orbit can be understood and accounted for.

FIG. 2. The IRIS model concept



Lenticular Structure

The lenticular structure is the principal component of IRIS. Its purpose is to function as a reflector, concentrator, or both, as in a Power Antenna. Figure 3 illustrates the shape and design of the entire lenticular structure. The other systems are not discussed here, although the reader is referred to an Interoffice Memorandum prepared by the team on the design and development of the IRIS model, which is available upon request from JPL. (See References).

The lenticular structure is made of two symmetric paraboloids, each with 12 gores, mated by means of a common annulus. One side is aluminized, acting as a reflecting surface; the other is clear, providing support for the lenticular structure.

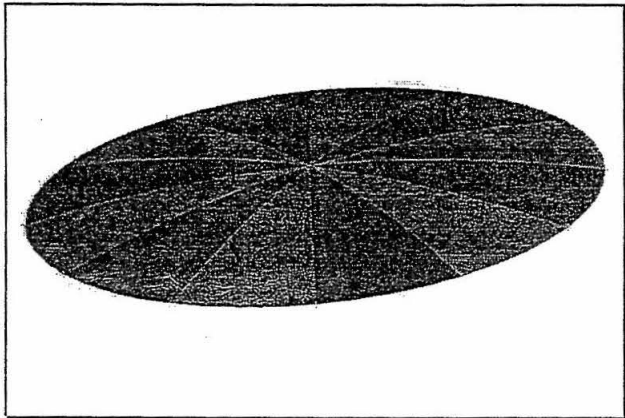


FIG. 3. 3-D view of lenticular structure

Design

The lenticular structure was designed to have a diameter and focal length of 2 m. This produced a focal length/diameter (f/D) ratio of 1, simplifying the fabrication of the model. The equation governing the parabolic shape of the lenticular structure is:

$$y = \left(\frac{1}{4f}\right)x^2 \quad (1)$$

In this model, the focal length of 2 m results in the following equation:

$$y = \left(\frac{1}{8}\right)x^2 \quad (2)$$

The annulus was constructed from tarp (4 mil thick), purchased from Home Depot. The purpose of using an annulus is to provide support and balance stress on both paraboloid shapes (aluminized and clear sides) due to inflatant pressure, and to leave extra material to attach the lenticular structure to the torus. Thus the annulus was

designed to have a 1 m inner radius and a width of 2.5 cm, giving it an approximate outer radius of 1.025 m.

Following advice from L'Garde and JPL engineers, it was clear that attaching two circular patterns of different material would not result in the correct lenticular shape upon inflation. The challenge in the design phase of the lenticular structure consisted of determining a gore size and shape that would yield the correct form when constructed and inflated. Due to proprietary reasons, L'Garde was unable to provide information or algorithms for determining the gore shape. It was thus necessary to design the gore pattern. At the suggestion of L'Garde, the IRIS team decided to construct on-axis symmetrical design of 12 gores and a center cap for each of the paraboloids, an adequate approximation.

The main difficulty was transforming a 2-dimensional membrane into a 3-dimensional structure. Since a membrane can bend in only one direction without wrinkling, simultaneous curvature cannot be obtained in both the radial and circumferential directions. The devised solution was to split the membrane up into gores. A method for calculating the width of the gore as a function of length along the gore was used, as seen in Figure 4. (Detailed mathematical calculations are available upon request from JPL). Curving radially, not circumferentially, the final structure would be a close approximation to the actual paraboloid.

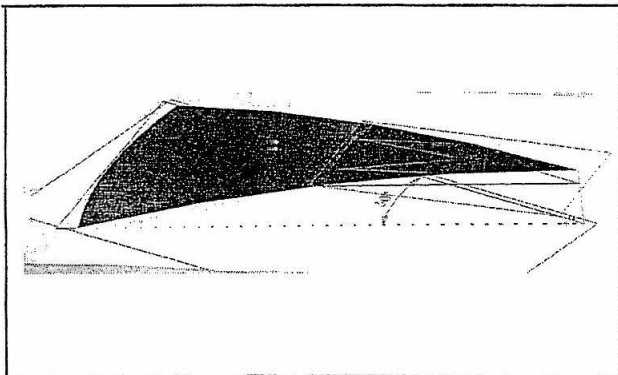


FIG. 4. Visual representation of method used to calculate gore width

A circle of 12.5 cm outer radius and 10.0 cm inner radius from the tip of the gores was drawn on the template to reduce adhesive crowding from tape overlap in the middle of the paraboloid. Tom Rivellini at JPL advised the use of a circular centerpiece roughly 1/8 the diameter of the annulus to attach the gores. Thus, a 0.25 m diameter was selected for simplicity of construction. Figure 8 depicts the template of the final gore pattern used for construction of the lenticular structure.

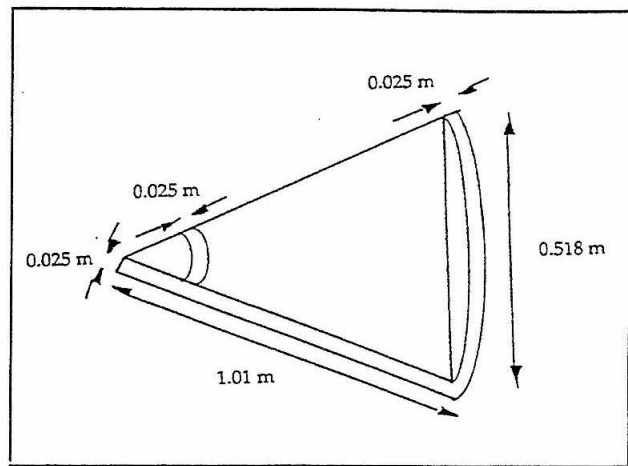


FIG. 5. Gore template

Construction

Having selected the materials to work with, the next problem encountered was connecting the gores to make a parabolic lenticular structure. A template of the gore shape was devised, printed out, and traced onto a hard cardboard surface using Integrated Design Engineering Analysis Software (I-DEAS). A mandrel was constructed to match the parabolic shape illustrated in Figure 6.

Specific problems encountered included lining up the gores and combining all 12 individual gores into the 3-dimensional lenticular structure and working with delicate materials like Mylar.

The lenticular structure performed extremely well at JPL Open House with no noticeable leakage. The volume of the lenticular structure was determined on I-DEAS to be 0.393 m^3 and inflated to approximately 3 psi in roughly 8 minutes.

Recommendations

- Further investigate the correct analytical model of the gore pattern.
- Verify the material strengths of the samples used and determine analytically, as well as experimentally, the pressure requirements of the lenticular structure.
- Construct a full-size mandrel of the lenticular structure. Although possibly difficult and expensive to construct, such a mandrel would significantly aid construction and improve the accuracy of the parabolic lenticular shape.

Conclusion

Although there were some significant problems faced in building this model inflatable structure, the design, development, and construction of a conventional antenna would likely be more time consuming and a lot more expensive. The use of inflatable structures in aerospace and planetary applications is realistic and achievable. The potential benefits of Power Antennas are very fascinating and pose challenging engineering problems. For instance, since both telecommunications-subsystem-specific power (bits/s/watt) and solar photovoltaic power output (watts) are independent parameters that scale with reflector area, Power Antenna communications data rates scale roughly as the fourth power of reflector! One could imagine an enormous telecommunications capability for large inflatable antennas. For example, a 150 kg Power Antenna system at a distance of ~20 AU from the Sun is predicted to downlink to the Deep Space Network at a rate of 100 kb/s. Conventional fixed antenna spacecraft could deliver at a rate of 3 kb/s for the same combined power and telecommunications subsystem masses. Figure 6 illustrates the benefits of the inflatable Power Antenna over conventional models.

Serious interest and funding from the user community will increase provided realistic demonstrations of this advanced and exciting technology continue.

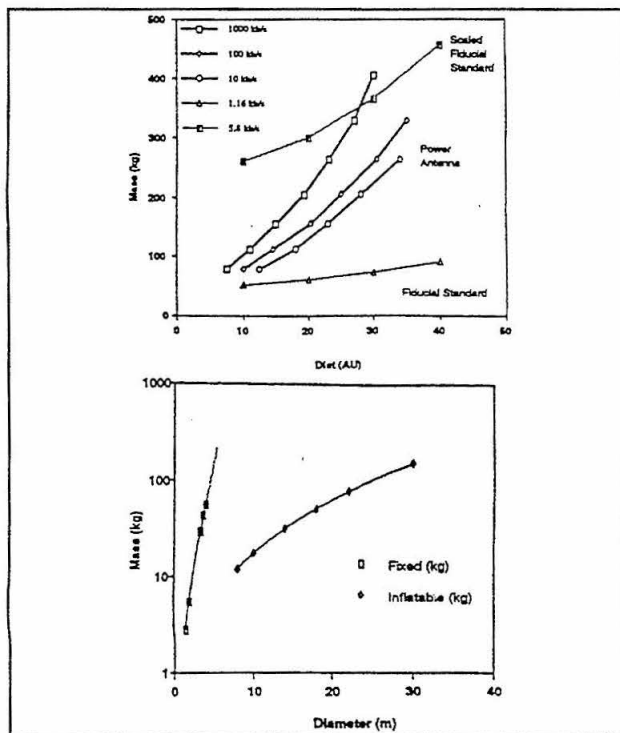


FIG. 6. Comparison of inflatable antenna parameters with those of conventional antennas

The IRIS project was constructed by seven students who worked at JPL during the summer of 1995 as students of the New Millennium Program. They are: Amir Alagheband, Maud Courtois, Roopesh Doshi, Farouk Hadeed, Donald Kwak, Laura Munoz, and Daniel Thunnissen.

References

1. Alagheband, A., Courtois, M., Doshi, R., Hadeed, F., Kwak, D., Munoz, L., & Thunnissen, D. (1995). The Design and Development of the Inflatable Reflecting Integrated Structure (IRIS). *JPL InterOffice Memorandum 3500-95-DT-01 (NASA)*. August.
2. Cassapakis, C. (1995) Conversation at L'Garde Inc. July.
3. Friese, G., Bilyeau, G., Thomas, M. (1983). Initial '80's Development of Inflated Antennas. *NASA CR 166060*. January.
4. Kroschwitz, J. (1987). *Polymers: An Encyclopedic Sourcebook of Engineering Properties*. John Wiley & Sons.
5. Mikulas, M. (1995). *Material Characterization for Rigidizable Deployables*. Presented at L'Garde Inc, Tustin, California. July 24.
6. Sercel J. (1995). Power Antenna Technology. *JPL document D-12685 (NASA)*. To be released.
7. Thunnissen, D., Engelbrecht, C., Webster, M. (1995). Low Mass Inflation System for Inflatable Structures. *JPL Interoffice Memorandum (NASA)*. June.
8. Waterman, N. & Ashby, M. (1991). *CRC-Elsevier Materials Selector*. CRC Press. Vol. 3.
9. Willis, P. (1995). Materials Challenges in Space Inflatable Structures. *Space Applications of Thin Films and Fabrics Miniconference*. May 8.